Multimodal calyceal innervation of the extended amygdala by pontine Kölliker-Fuse PACAPergic neurons

Limei Zhang[1, 2†*], Vito S. Hernández[1, 2†], David M. Giraldo[3, 4], Sunny Z. Jiang[2], Juan C. León-Contreras[5], Rong Ye[6], Shiliang Zhang[6], Martin K-H Schäfer[7], Rafael A. Barrio[8], Rogelio Hernández-Pando[5], Francesco Ferraguti[9] and Lee E. Eiden[2]

[1]Department of Physiology, School of Medicine, National Autonomous University of Mexico (UNAM)

[2]Section on Molecular Neuroscience, National Institute of Mental Health, NIH, USA.

[3]Microscopy Core, School of Medicine, UNAM, Mexico City Mexico.

[4] ZEISS Innovation Center, Carl Zeiss Microscopy, LLC, Dublin, California, USA

[5]Department of Experimental Pathology, National Institute of Medical Sciences and Nutrition "Dr. Salvador Zubirán", Mexico City, Mexico

[6]Confocal and Electron Microscopy Core, National Institute on Drug Abuse, NIH, USA.

[7]Center for Mind, Brain and Behavior, Philipps University of Marburg, Germany.

[8]Department of Complex Systems, Institute of Physics, UNAM, Mexico City, Mexico.

[9]Institute of Pharmacology, Medical University of Innsbruck, Innsbruck, Austria.

[†]Sabbatical researcher; *Correspondence: limei@unam.mx

Abstract: The calyx of Held is a giant, excitatory, cup-like axo-somatic synapse in the auditory brainstem and the only synapse of its kind described in the central nervous system. Here, using PACAP immunohistochemistry combined with confocal and tomographic electron microscopy, we report the discovery of a morphologically analogous calyx-like synapse in the rodent forebrain extended amygdala that exhibits unique neurochemical and structural features. This previously unrecognized terminal forms an enveloping axo-somatic specialization with mixed glutamatergic and cholinergic identities, co-expressing VGluT1, VGluT2, VAChT, and the neuropeptides PACAP, CGRP, and neurotensin, together with calretinin in the presynaptic compartment. We identified a distinct neuronal subpopulation in the pontine Kölliker–Fuse (KF) region of the parabrachial complex that gives rise to these calyceal terminals, which engulf PKCδ$^+$/GluD1$^+$ somata in the capsular central amygdala and oval BNST. Strikingly, GluD1 immunolabeling is concentrated at axo-somatic contact zones apposed to VAChT$^+$ active zones but is absent from postsynaptic densities of conventional type I synapses within the same terminals. Our findings reveal a previously unrecognized multimodal calyx-like synapse in the forebrain, demonstrating the convergence of fast and modulatory transmission mechanisms and suggesting a structural substrate for high-fidelity signal integration within viscerosensory–emotional circuits.

Significance Statement: High-fidelity axo-somatic synapses, exemplified by the calyx of Held in the auditory brainstem, have never been demonstrated in the forebrain. Here we identify a multimodal calyceal synapse in the extended amygdala formed by PACAPergic neurons of the pontine Kölliker–Fuse nucleus. These giant terminals co-package glutamate, acetylcholine, and multiple neuropeptides, enveloping PKCδ$^+$/GluD1$^+$ neurons in the capsular central amygdala and oval BNST. This discovery expands the structural repertoire of forebrain synapses and reveals a direct anatomical substrate linking viscerosensory input from the hindbrain to limbic autonomic centers. Such high-fidelity multimodal transmission may underlie the precise synchronization of emotional and homeostatic control circuits.

Key words: Calyx of Held, axo-somatic synapse, FIB-SEM, TEM, multi-transmitters, co-transmission, neuropeptides, GluD1, PKCd

Introduction

Precise and high-fidelity neurotransmission is a hallmark of certain specialized synaptic architectures in the mammalian brain. One of the most striking examples is the calyx of Held, a giant axo-somatic glutamatergic terminal in the auditory brainstem [1], first described over a century ago by Hans Held [2]. This unique synapse, formed by globular bushy cells onto principal neurons in the medial nucleus of the trapezoid body (MNTB), is characterized by its expansive presynaptic terminal that engulfs the soma of its postsynaptic target, supporting fast, one-to-one spike transmission with minimal delay and jitter [1, 3, 4]. The structure and function of the calyx of Held have provided a foundational model for understanding synaptic reliability, vesicle dynamics, and temporal precision in sensory circuits [5].

While previous studies have noted that some features of calyx synapses can be observed in hippocampal mossy fiber boutons and cerebellar climbing fiber terminals [6], these structures predominantly target dendrites and do not fully recapitulate the enveloping, axo-somatic morphology characteristic of the calyx of Held. Similarly, earlier reports describing basket-like axosomatic contacts formed by neuropeptide calcitonin gene-related peptide (CGRP) [7, 8] [9, 10], pituitary adenylate cyclase activating polypeptide (PACAP) [11], neurotensin [12] and reportedly forming type II axo-somatic synapses under transmission electron microscopy [9, 10, 13], have not demonstrated that these terminals engulf their postsynaptic targets. Therefore, to our knowledge, a fully enveloping calyx-like synapse has not yet been described at ultrastructural level in forebrain circuits.

The extended amygdala, comprising the capsular central amygdala (CeC) and bed nucleus of the stria terminalis oval (BSTov), serves as a crucial hub for rapid viscerosensory processing and for coordinating autonomic, behavioral and emotional responses to threats and homeostatic challenges [14, 15]. These interconnected nuclei receive robust brainstem inputs carrying visceral and nociceptive information, notably from the parabrachial nucleus (PBN) – which alert the extended amygdala to internal bodily states and imminent threats [13, 16, 17]. Within the extended amygdala, PKCδ^+ GABAergic neurons in CeL/CeC inhibit GABAergic output neurons in medial CeA (CeM), establishing a local disinhibition motif that gates downstream autonomic pathways [18]. These latter ones have been shown through anterograde tracer and electron microscopy (EM) that monosynaptically innervate the rostral ventrolateral medulla sympathetic center (RVLM), including appositions onto phenylethanolamine-N-methyltransferase neurons that were Fos-positive after hypotension. Beyond the amygdala, CeA and BNST GABAergic projections modulate PVN activity indirectly via the peri-PVN GABAergic zone, which provides tonic inhibition to hypothalamic paraventricular nucleus (PVN) via a peri-PVN GABAergic shell hence is predicted to disinhibit PVN [19]. In this framework, activation of PKCδ^+ CeC/BSTov neurons would inhibit local CeM output as well as pPVN GABA neurons, lifting inhibitory tone onto sympathetic-promoting hypothalamic/medullary circuits. Recent functional work using a hydralazine-induced hypotension model shows that this parabrachial–extended amygdala axis is recruited early, before hypothalamic magnocellular activation, consistent with a role in rapid autonomic compensation [20].

Among the brainstem sources that inform the extended amygdala, the parabrachial complex (PBc) is a laminated pontine hub for interoceptive and nociceptive signals. Classic tract-tracing studies established that neurons in the lateral parabrachial nucleus (LPB), particularly the external/lateral subdivisions send dense rostral projections to the capsular central amygdala (CeC) and the oval BNST (BSTov), providing a major viscerosensory relay to limbic autonomic circuits [7, 9, 16, 21-24] [25]. Within the PBc, the Kölliker–Fuse (KF) forms a ventrolateral sector at the pontine-mesencephalic junction that interfaces respiratory and autonomic control, and KF/LPB neurons with glutamatergic and PACAP phenotypes contribute to the PB-EA stream[20]. Thus, anatomically and neurochemically, PBc outputs-LPB and KF-are well positioned to deliver rapid interoceptive drive to PKCδ-centered EA microcircuits implicated in sympathetic regulation [23]. Contemporary neurochemical work further emphasizes the KF's mixed glutamatergic/neuromodulatory makeup and autonomic–respiratory roles, consistent with a fast interoceptive drive into EA [26].

Despite its pivotal role in homeostatic and stress regulation, the ultrastructural organization of its long-range inputs to central amygdala remains poorly understood. Here we describe a multimodal calyx-like synapse originating from PACAP-rich neurons in the pontine Kölliker–Fuse nucleus, representing the first forebrain example of a calyceal-type terminal. Using confocal and transmission and tomographic electron microscopy combined with cell-type-specific tracing, we show that this giant axo-somatic terminal co-packages markers for glutamate, acetylcholine, and multiple neuropeptides, and envelops PKCδ^{+}/GluD1^{+} neurons within the EA. This discovery reveals a new morphological and neurochemical substrate through which the hindbrain can deliver rapid, high-impact viscerosensory signals to limbic autonomic circuits.

Results

PACAP-Containing ring-like structures identified in the Forebrain. To assess the distribution of PACAP containing inputs in the rodent telencephalon, we performed immunohistochemistry and identified a highly selective ring-like innervation pattern in distinct forebrain regions. These perisomatic PACAP-positive structures were especially prominent in the capsular subdivision of the central amygdala, (CeC), the oval nucleus of the bed nucleus of stria terminalis (BSTov), and to a lesser extent, scattered within the dorsal and ventral subdivisions of the lateral septal nucleus (see Supplemental Fig. 1). Within the amygdaloid complex (Fig. 1, panels As and Bs), we observed heterogeneous PACAP immunoreactivity across multiple amygdaloid nuclei. A dense mesh of fine, varicose PACAP-immunoreactive (PACAP-ir) fibers was distributed in the lateral amygdala (LA, Fig. 1, A and B, B2), postero-dorsal medial amygdala (MePD, Fig. 1, A and B, and B4), posteroventral amygdala (MePV, Fig. 1 B), basolateral (BLA), and basomedial amygdala (BMA, Fig. 1, A and B, B3) amygdala, as well as in the central lateral (CeL) and central medial (CeM) subdivisions of the amygdala (Fig. 1, A and B, B1) forming diffuse *en passant* type

innervation patterns. In contrast, the CeC displayed a population of thicker, non-varicose PACAP+ fibers forming distinct ring-like axo-somatic arrangements around a subpopulation of neurons (Fig. 1, A, A1, B, and B1, arrows).

Neuroanatomical Characterization of PACAP+ Calyceal Terminals. To determine the postsynaptic target of these PACAP containing rings, we first assessed somatostatin (SST)-expressing neurons, but these lacked expression of the PAC1 receptor (SI Figure 2, panel A). Since both the CeC and BSTov are known to also contain a high density of PKCδ-expressing neurons [27, 28], we assessed this population first with RNAscope multiplex method, finding that a subpopulation of *Prkcd* expressing neurons mainly located in the ventro-lateral segment of CeC co-expressed *Adcyap1r1* (PAC1,) *Grid1* (GluD1), *Chrna7* (nAChRa7) (SI Figure 2, B). Using a *Prkcd*-Cre::Ai9 double transgenic mice, in which PKCδ-+ neurons are fluorescently labeled with TdTomato, we detail the distinct morphological features of the PACAP-immunoreactive axonal terminals in the CeC, particularly enriched in its postero-ventro-lateral region (Fig. 1 C). These terminals display a perisomatic "calyx-like" arrangement, as seen in high-magnification confocal images (Fig. 1, C1), and juxtapose with GluD1-immunolabeled domains of PKCδ expressing neurons (Fig. 1, D), supporting a direct axo-somatic PACAP containing input onto PKCδ+/GluD1+ neurons.

Figure 1. PACAP immunopositive fibers form perisomatic ring-like innervation patterns targeting PKCδ neurons in the capsular division of the central amygdala (CeC). (A–B) Coronal sections of the rat amygdaloid complex immunostained for PACAP (PACAP-ir). Blue dashed outlines indicate subdivisions of the amygdaloid nuclei, including CeC (capsular), CeL (lateral), CeM (medial), BLA (basolateral), BMA (basomedial), LA (lateral), and MePD/MePV(posterodorsal/posteroventral medial amygdala). (A, A1) Contralateral amygdaloid complex at approximately bregma −1.46 mm. Blue-black arrowheads highlight ring-like PACAP-ir structures predominantly in the ventral portion of the CeC. (B) Amygdaloid complex at bregma −1.70 mm, where ring-like PACAP+ structures are observed exclusively in the CeC. (B1) Higher magnification of the boxed CeC region in panel B. (B2–B4) Representative PACAP-ir fibers with varicosities (*en passant* type) indicated by black arrows. (C) Horizontal section from a Prkcd-Cre::Ai9 mouse showing tdTomato-labeled PKCδ+ neurons (red) and PACAP immunostaining (green) in the CeC. (C1) Higher magnification of the caudal CeC reveals abundant PACAP-ir perisomatic rings around PKCδ+ cells, mainly located in the posterolateral portion of this horizontal plane. (D) High-resolution immunofluorescence for PACAP (blue), GluD1 (green), and PKCδ–Ai9–tdTomato (red) highlights PACAP-ir labeling around PKCδ+ somata, with GluD1 signals localized to membrane regions in close apposition to PACAP+ elements. (Figure 1 displayed in next page)

Figure 1 (caption in previous page)

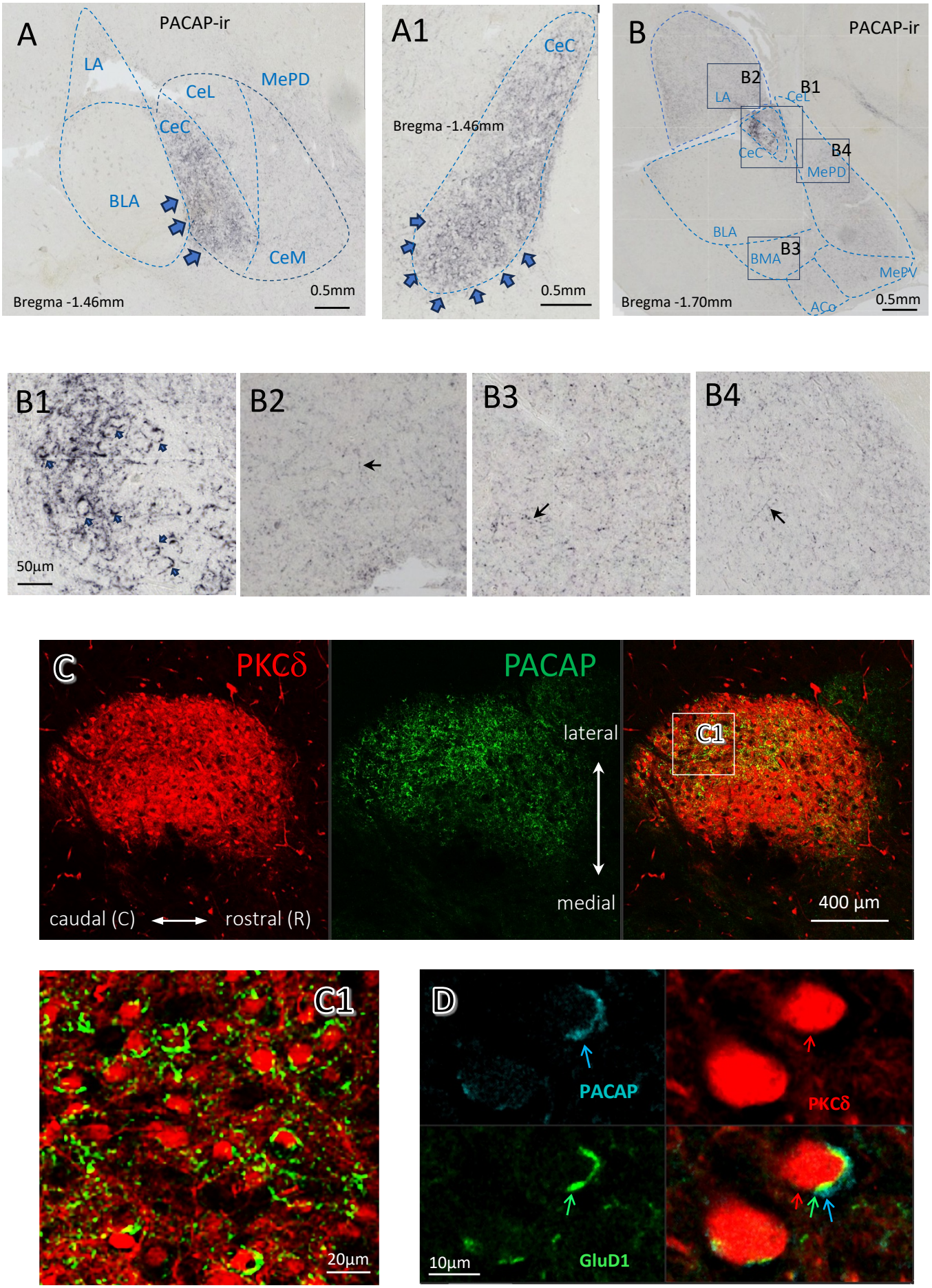

Electrophysiological analysis of PACAP-driven responses. In order to determine the postsynaptic response of PKCδ-expressing neurons in the CeC to PACAP, we performed *ex vivo* whole-cell patch-clamp recordings in brain slices from Prkcd-Cre::Ai9 mice, in which PKCδ+ neurons are labeled with TdTomato. Recordings were conducted in artificial cerebrospinal fluid (ACSF) with a 100 nM PACAP bath application followed by a washout period (Fig. 2). We report that whole-cell patch-clamp recordings from PKCδ+ neurons reveal two functionally distinct subtypes. Type 1 neurons (symbolized with red dots in Fig. 2, panel A, N=21, located in the ventro-lateral segment of CeC) show a robust and reversible increase in firing rate during PACAP application (Fig. 2, panel B), along with a steeper current–frequency (I–F) relationship (Fig. 2, C), while type 2 neurons (symbolized with black dots in panel A, N=9) exhibit no significant change in excitability (Fig. 2, E). For PACAP-responsive neurons (type 1), a two-way ANOVA revealed significant main effects of treatment, $F(2,780) = 25.64$, $p < 0.001$, and current injection steps, $F(12,780) = 298$, $p < 0.001$, with no significant interaction between the factors. *Post hoc* multiple comparisons confirmed a significant increase in excitability during PACAP application relative to baseline ($p < 0.001$), with firing rates returning to baseline levels during the washout (no significant difference compared to ACSF condition). Furthermore, *post hoc* immunohistochemistry demonstrated that these PACAP-responsive neurons expressed GluD1 at the plasma membrane (Fig. 2D, left panel), and their morphology was confirmed by biocytin filling (Fig. 2D, right panel). These characteristics are consistent with the PACAP-containing axons perisomatically innervating a subpopulation of PKCδ+ neurons described in Figure 1. Interestingly, long projecting axons of the type 1 neurons were observed (Fig. 2D, right panel, main axon was indicated by arrows). The type 2 neurons (symbolized with gray circles, N=9, Fig. 2A) showed no significant change in firing frequency during PACAP application (Fig. 2E–F). The two-way ANOVA for Type 2 neurons revealed a significant effect of current injection steps, $F(12,312) = 84.1$, $p < 0.001$, but no significant effect of treatment, $F(2,312) = 0.606$, $p > 0.05$, nor any significant interaction between the factors. Post hoc analysis confirmed no differences in firing rate under ACSF, during PACAP application, or during the washout period. Additionally, these PACAP-insensitive neurons lacked membrane-localized GluD1 despite being TdTomato-expressing (Fig. 2F, left panel), and their morphology was similarly confirmed via biocytin labeling (Fig. 2F, right panel).

Figure 2 (caption in next page)

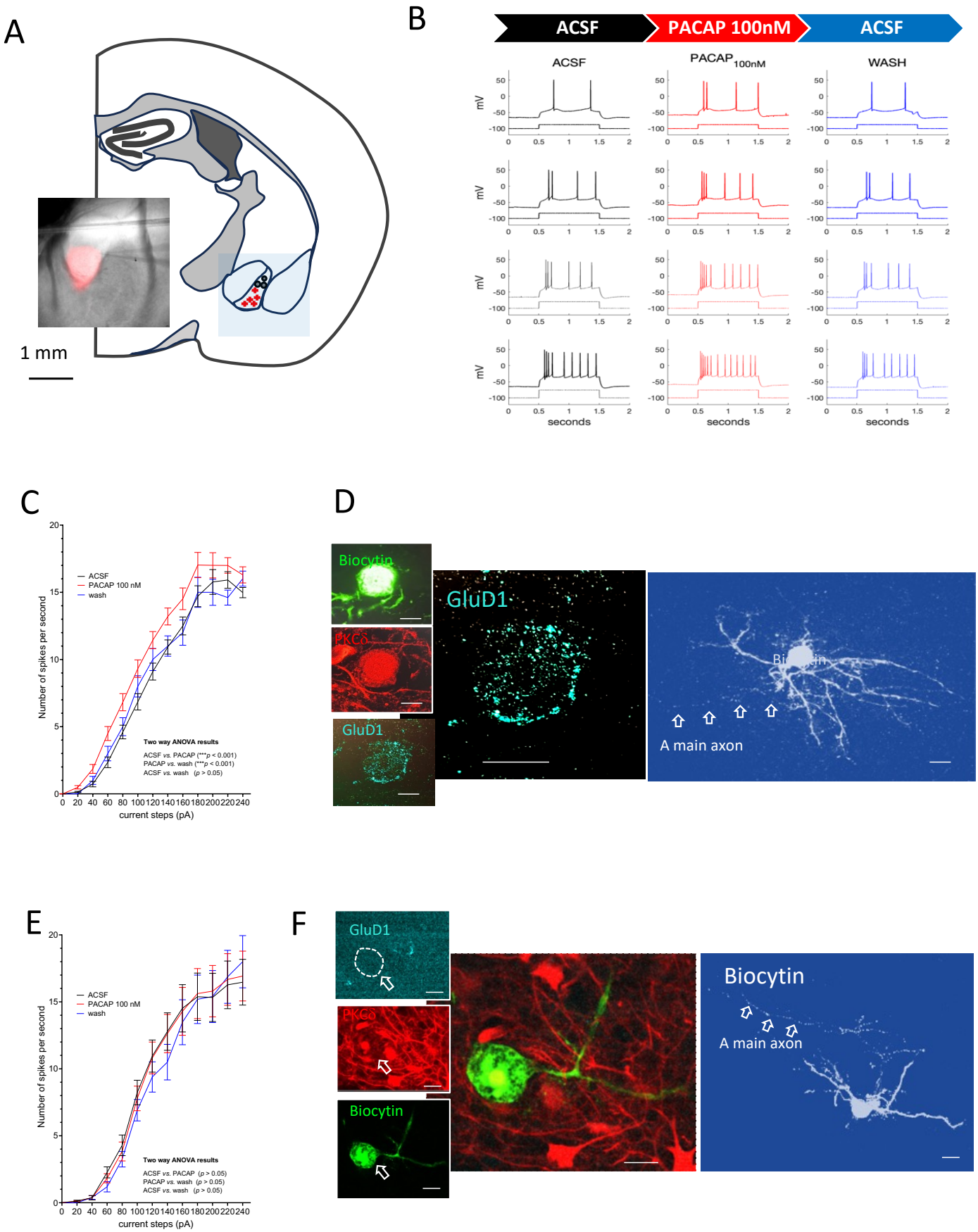

Figure 2. Whole-cell patch-clamp recordings reveal both PACAP-sensitive and PACAP-insensitive subtypes of PKCδ+ neurons in the central amygdala (CeA). (A) Schematic of ex vivo recordings performed on horizontal brain slices from Prkcd-Cre::Ai9 mice, illustrating TdTomato-labeled PKCδ+ neurons in the capsular division of the CeA (CeC) red crosses symbolize the type 1 PKCδ+ cells, while the grey circles symbolized the type 2 PKCδ+ (vide infra). (B) Representative current-clamp traces from a PACAP-sensitive (type 1) neuron showing increased firing in response to 100 nM PACAP (red), which returns to baseline after washout (blue). (C) Current–frequency (I–F) curves demonstrating enhanced excitability of type 1 neurons during PACAP application (red curve, n = 21), a two-way ANOVA revealed significant main effects of treatment, $F(2,780) = 25.64$, $p < 0.001$. After a 10 min period of washout (blue curve), no significant differences were observed compared to the excitability curve before PACAP application (black curve). (D) Example of a type 1 cell with post hoc immunofluorescence that confirms GluD1 expression (cyan) localized to its plasma membrane (left) and biocytin labeling and its dendritic morphology and axonal projection (right). (E) In contrast, PACAP-insensitive (type 2) neurons (n=9) show no change in firing frequency following PACAP application (red curve), no significant effects of treatment were shown in the two-way ANOVA. (F) Post hoc analysis of these Type 2 cells reveals the absence of GluD1 membrane expression (left) despite successful biocytin filling (right). Scale bars: 10 µm.

Molecular signature of calyceal terminals engulfing the PKCd-ir neurons in CeC. We then decided to delve further into the molecular architecture of these large perisomatic PACAP+ terminals. High-resolution confocal imaging revealed that these ring-like axon terminals co-expressed the vesicular glutamate transporter 1 (VGluT1) and/or 2 (VGluT2) (Fig. 3, panel D, A11, 12, A17, B6 y B7 and Fig. 5 panel H, at electron microscopy level), analogously to the calyx of Held in the medial nucleus of trapezoid body (MNTB), and the vesicular acetylcholine transporter VAChT (Fig. 3, panels B). Furthermore, the presynaptic PACAP+ rings around the somata of PKCd-expressing neurons contained the neuropeptides calcitonin-gene related peptide (CGRP) and neurotensin (NTs), as well as the calcium binding protein calretinin (Fig. 3, panels C). These findings indicate a multimodal transmitter phenotype for these axon terminals that include glutamatergic, cholinergic, and peptidergic components. To prove that their spatial organization is similar to that of a calyx of Held (calyx-like), we performed confocal z-stacks of PKCd-expressing neurons segmentation in the CeC. The PACAP+ fibers formed large cup-like, enveloping axo-somatic terminals, confirming their calyx-like macro-architecture (Fig. 3, D).

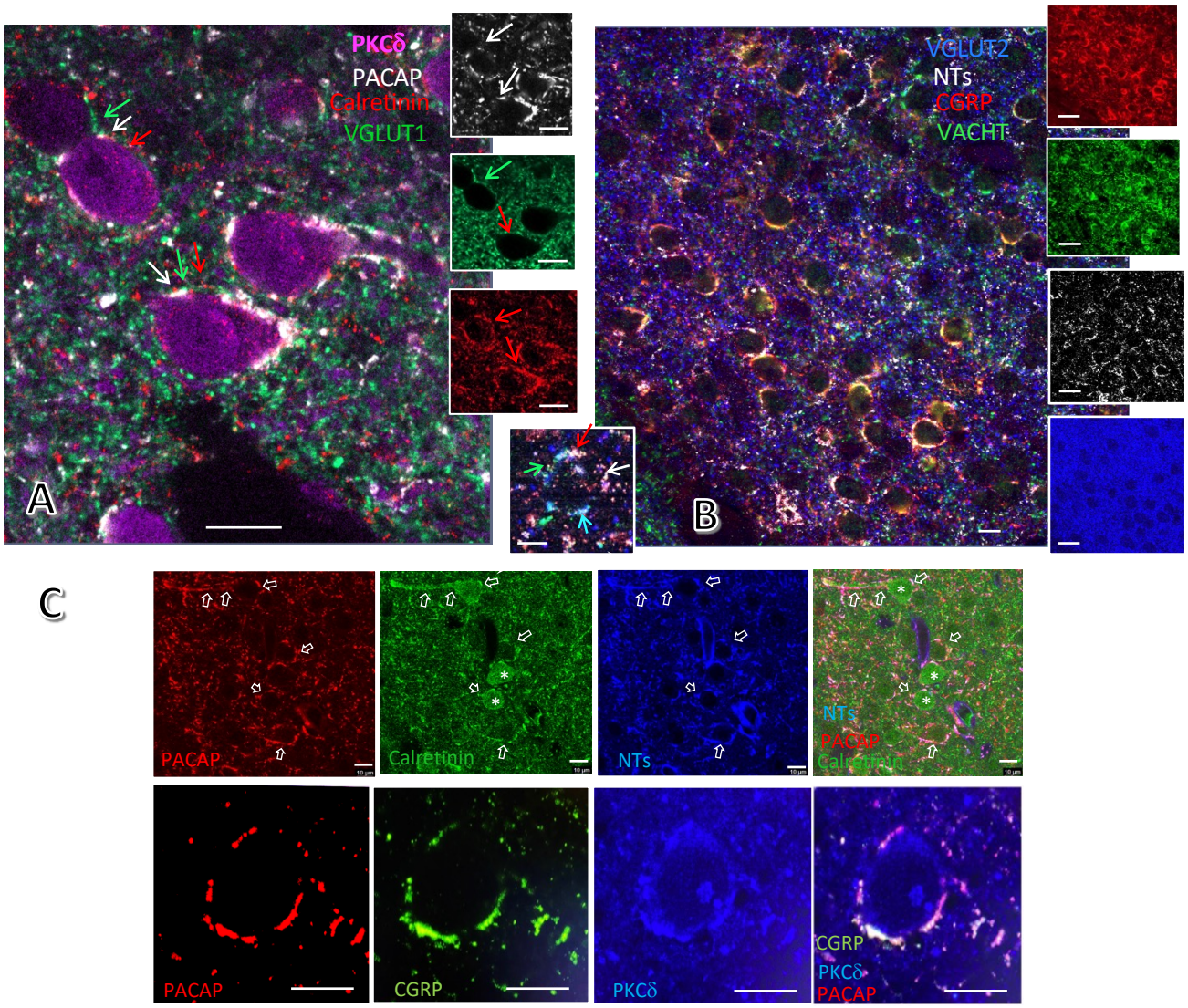
PKCδ
PACAP
Calretinin
VGLUT1
A
VGLUT2
NTs
CGRP
VACHT
B
C
PACAP
Calretinin
NTs
PACAP
Calretinin
PACAP
CGRP
PKCδ
CGRP
PKCδ
PACAP

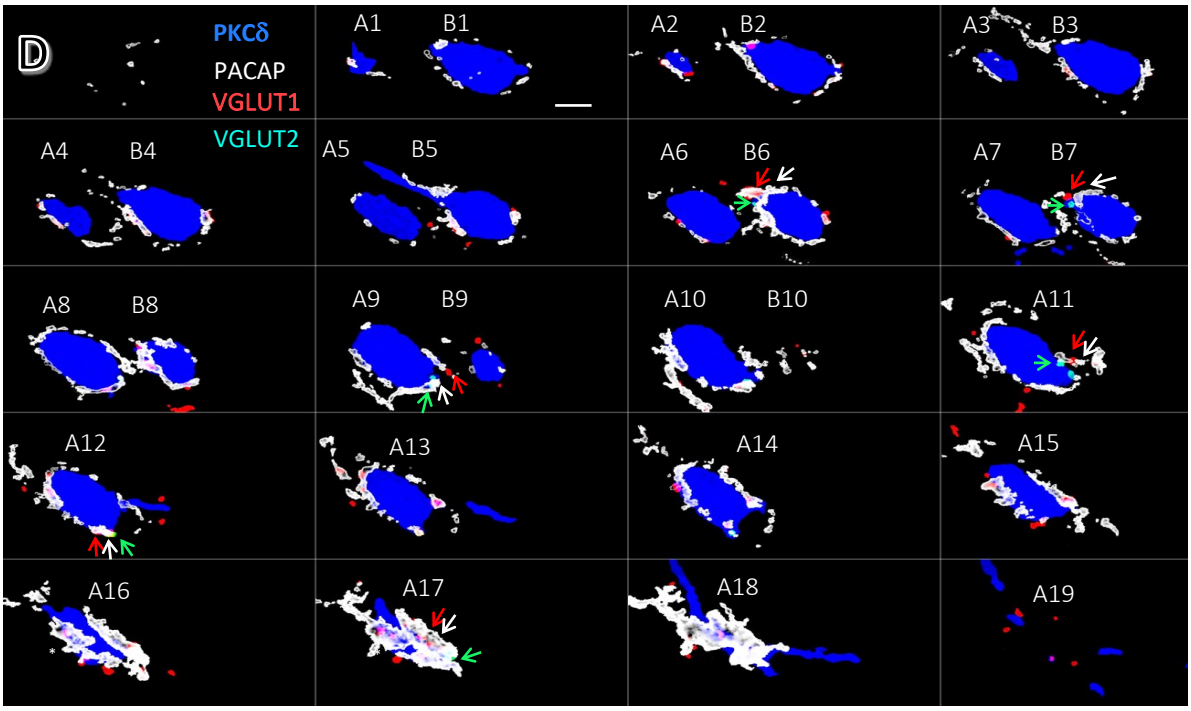
D
PKCδ
PACAP
VGLUT1
VGLUT2
A1 B1
A2 B2
A3 B3
A4 B4
A5 B5
A6 B6
A7 B7
A8 B8
A9 B9
A10 B10
A11
A12
A13
A14
A15
A16
A17
A18
A19

Figure 3: Neurochemical composition of the ring-like structure in the CeC: A and B: High-magnification confocal views demonstrate that these perisomatic structures co-express multiple markers, including in A: VGluT1 (green labeling), calretinin (red labeling), PACAP (white labeling) and PKCδ (pink labeling); B: neurotensin (NTs, white labeling), vesicular acetylcholine transporter (VAChT, green labeling), VGluT2 (cyan labeling), and calcitonin gene-related peptide (CGRP red labeling). C: top row, co-expression of neuropeptides NTs (blue), PACAP (red) and calcium binding protein calretinin forming ring-like structure. Note that some targeted neurons are calretinin expressing (*). In one case, NTs/PACAP/calretinin co-expressed axon approached the targeted cell guided by its main dendrite (arrows at the top part of the panels). Bottom row: ring structure with PACAP/CGRP co-expression engulfing a PKCδ expressing neuron. D. Segmentation of 20 serial confocal optical sections of two PKCδ-expressing neurons of rat CeC (blue) illustrates the spatial organization of two VGluT1, VGluT2, PACAP co-expressing ring-like fibers surrounding their somata. Scale bars: 20μm.

Ultrastructure of the extended-amygdala calyceal synapse (EM level). Serial FIB-SEM tomography (20 × 20 × 20 nm voxels; Fig. 4A) of PACAP immunoreacted CeC sample revealed a single, giant presynaptic terminal that engulfs the somatic surface of its postsynaptic neuron. Three-dimensional reconstructions show a cup-like shell perforated by 40–50 slender filopodial protrusions that track the contour of the target soma (Fig. 4, panel A2, A3 and A4). Inside the calyceal lumen, the postsynaptic membrane is smooth and devoid of spines, reminiscent of the principal cell in the classical calyx of Held (Fig. 4, A1, also see the supplemental information videos 1, 2, 3)

At higher magnification (Fig. 4, B,C), multiple synaptic specializations (SS) can be observed within the calyceal structure (indicated with arrowheads). The active zones of those SS are packed with membrane bound clear, round vesicles and scattered large dense-core vesicles (indicated by white asterisks) that immunoreacted for PACAP. Mitochondria ("m" in panel B) are abundant within the calyceal structure. We revealed that PACAP-ir calyceal terminal formed both asymmetric (type I) and symmetric (type II) synaptic contacts (Fig. 4C), a higher prevalence of type II configurations (Fig. 4D). This type II SS showed strong deposition of electron dense materials in the presynaptic active zone coincided with vesicular Ach transport (VAchT) immunolabeling (Fig. 4E, "*" indicate DAB deposition linked with VAChT-ir and inset shows double immunofluorescence that GluD1 (green) labeled plasma membrane apposed with VAchT-ir parches in the outline of the cell (red). Hence, these are symmetrical SS of cholinergic type II synapses [29, 30]. Noteworthy, we often detected strong GluD1 immunogold labeling of the postsynaptic density (PSD) of the type II SS. Figure 4 panel E show an example of this calyceal synapse with mixed SS. The black arrowheads flank the type I SS, while the black arrowheads-outlined with red line flank the type II SS. Strikingly, the GluD1 immunolabeling (gold particles, indicated with black arrows) are selectively deposited in the PSD of the type II SS and only very few of them are deposited at the edge of the type I SS (red arrows) suggesting a specific molecular identity for this synaptic pairing. In SI Fig. 3, we show more examples (panels C, D, E, F and G) reinforcing the idea that GluD1 expression is closely associated with cholinergic inputs. The Glu1D has been interpreted as an adhesion molecule [31, 32] in recent literature. hence an

interesting question arises here that if this is the case, why is this selective distribution?, These findings support the notion that CeC-calyceal synapses represent a specialized subpopulation of central amygdalar connections, distinguished by their molecular profiles and potential neurotransmitter signaling mechanisms.

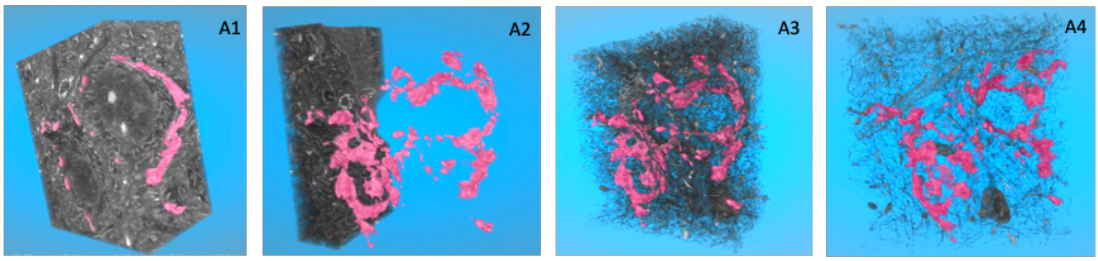

FIB-SEM
Video 1
Video 2
Video3

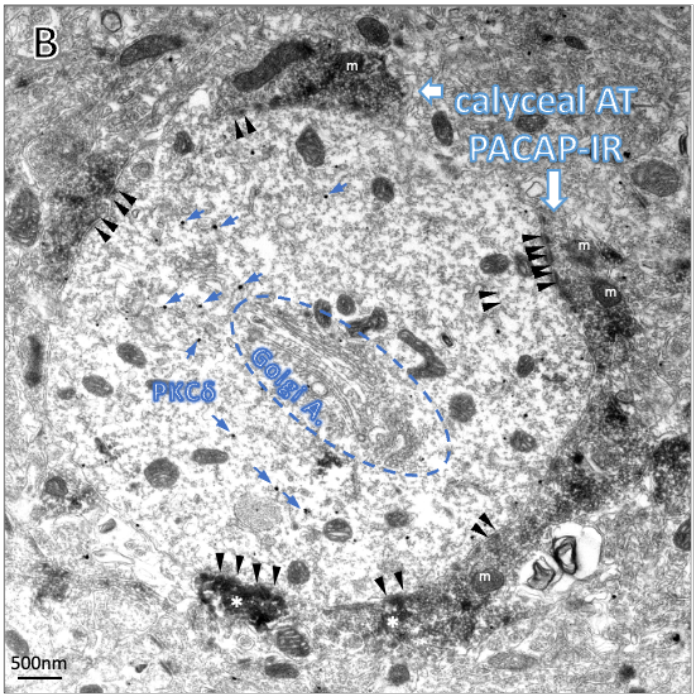

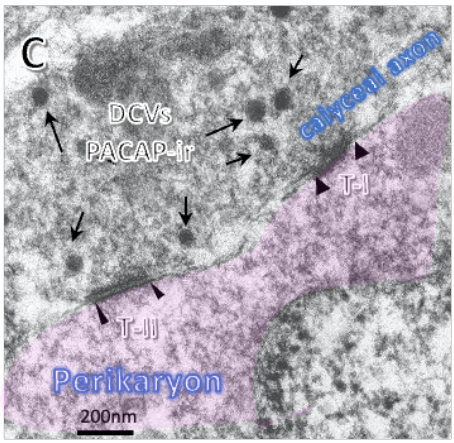

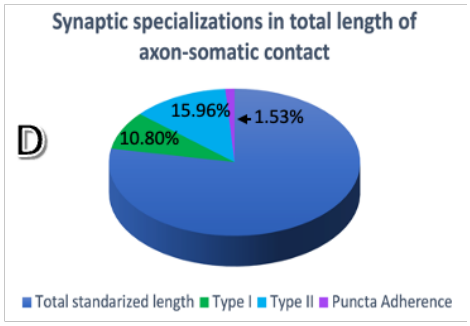

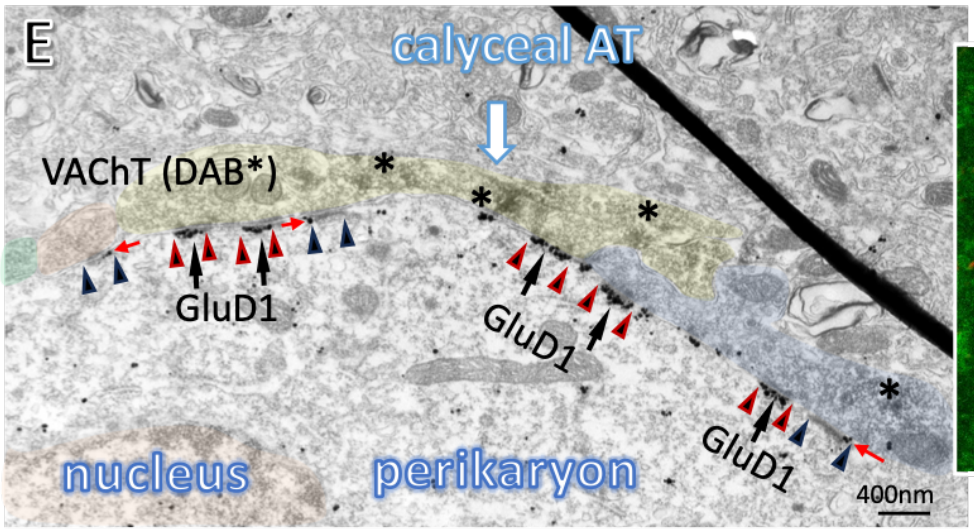

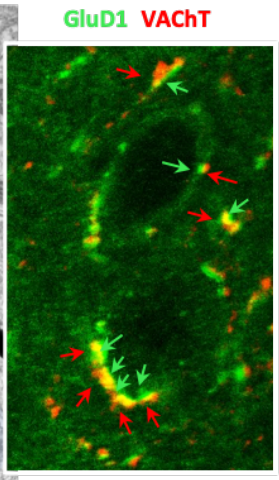

Figure 4. Electron microscopy showing distinct features of calyceal synapse in the extended amygdala. As:. A calyx of Held-like, ring-shaped synaptic structure in the central amygdala (CeC-calyceal synapse) revealed by immuno-electron microscopy against PACAP FIB-SEM (Focused Ion Beam Scanning Electron Microscopy). A1-A4: 3D reconstruction and segmentation of the same sample highlighting the ring-like morphology of the PACAP+ calyceal synapses. Corresponding video files showing the full reconstruction are available in the Supplemental Information videos 1, 2 and 3. B: a double-immuno-electron microscopy photomicrograph showing a PACAP-ir calyceal axon terminal formal numerous synaptic specifications (arrowheads) onto a PKCδ labeled (gold particles) soma (a Golgi apparatus was indicated). C. . A PACAP-expressing calyceal axon forms both asymmetric (type I, thick arrowheads) and symmetric (type II, narrow arrowheads) synaptic contacts. Presynaptic vesicles and both pre- and postsynaptic densities (PSDs) are visible. Arrows indicate PACAP+ dense core vesicles. D. A pie chart quantifies the proportion of each synapse type based on contact length measurements from randomly selected TEM micrographs (n = 30) in which synaptic specializations could be identified. E. Another example of a VAChT+ (* DAB) calyceal axon forming Type II synapses with GluD1-gold labeling at the post-synaptic density (PSDs). Note that the GluD1 gold particles are selectively located at the PSDs of type II synaptic specifications (red-black arrowheads). In contrast, the PSDs of 3 adjacent type I (asymmetric) synaptic specifications (black arrowheads) lack the GluD1 labeling. Inset: confocal image showing close spatial correspondence between VAChT (red) and GluD1 (green) signals. GluD1 expression is localized between the red VAChT-positive axon and the soma, suggesting a tight anatomo-functional association between cholinergic input and GluD1 expression.

Video 1: Serial imaging of PACAP immunopositive processes surrounding central amygdala neurons. Serial ultrastructural data were acquired using a Zeiss Crossbeam 550 focused ion beam–scanning electron microscope (FIB-SEM).

The dataset comprises 373 sequential images spanning a total depth of approximately 15 µm, yielding an effective z-step of ~40 nm between consecutive sections. Each image was recorded at an in-plane resolution of 10 nm per pixel, allowing isotropic three-dimensional reconstruction of subcellular architecture. Within this volume, we identified five adjacent cell bodies embedded in neuropil and surrounded by numerous PACAP-immunoreactive processes, which appear as electron-dense (dark) profiles surrounding the soma and proximal dendrites of local neurons. This high-resolution stack provides a detailed spatial framework for analyzing the organization of PACAP-containing elements in relation to neighboring cellular profiles.

Video 2. Three-dimensional reconstruction of PACAP-immunoreactive processes forming Calyxes with CeA neurons.

The electron-dense processes identified in Video 1 were segmented and rendered in three dimensions using DragonFly™ (Object Research Systems, Montreal, Canada). The reconstruction illustrates the spatial organization and continuity of these PACAP-positive elements, revealing their calyx-like morphology and close apposition to the surfaces of adjacent cell bodies. This

volumetric representation highlights the intricate anatomical relationships between the calyceal processes and surrounding cellular profiles, providing complementary visualization of the ultrastructural dataset acquired by FIB-SEM.

Video 3. Three-dimensional reconstruction of PACAP-immunoreactive calyx-like terminals contacting two neighboring cells.

A series of 488 consecutive FIB-SEM images (10 nm isotropic resolution in X, Y, and a Z step of ~ 40 nm) was used to reconstruct two adjacent cell bodies and their associated PACAP-positive axonal process. Segmentation and volumetric rendering were performed in DragonFly™ (Object Research Systems, Montreal, Canada). The reconstruction reveals a single PACAP-immunoreactive axon giving rise to calyx-like expansions that envelop the somatic membranes of both cells. Rotations of the model along different planes facilitate visualization of the three-dimensional geometry and the intimate anatomical relationship between the PACAP-containing calyx and the target somata.

Brain-stem origin of the calyceal input.

Stereotaxic deposits of the retrograde tracer Fluoro-Gold (FG) confined to the CeC (Fig. 5A1) labeled a discrete neuronal cluster in the ventrolateral parabrachial complex, centered in the Kölliker–Fuse (KF) nucleus (Fig. 5A,A2). Triple RNAscope applied to FG-filled neurons revealed that most retrogradely labeled cells co-expressed *Slc17a7* (VGluT1), *Slc17a6* (VGluT2), and *Adcyap1* (PACAP) mRNAs (Fig. 5A2–A5), indicating a glutamatergic/PACAP phenotype that matches the chemistry of the calyceal terminals identified in the EA. To test sufficiency, we injected a Cre-dependent AAV5-EF1α-DIO-hChR2(H134R)-eYFP into the KF of PACAP-Cre mice (Fig. 5B). Despite sparse transduction of only a handful of PACAP$^+$ somata per case, eYFP$^+$ axons produced stereotyped ring-like endings in both CeC and BSTov (Fig. 5B1–B3), recapitulating the perisomatic geometry seen with immunohistochemistry and in the rat juxtacellular reconstruction. Together, these results identify PACAP/VGluT1/VGluT2 KF neurons as a minimal presynaptic population capable of generating calyx-like terminals in the EA.

These anatomical data align with our rat study using hydralazine-evoked hypotension, where a single juxtacellularly labeled KF neuron sent a rostral axon through the superior cerebellar peduncle to dorsal tegmental bundle to the CeC, and continued via the ansa peduncularis to the BSTov, forming ring-like (calyceal-like) perisomatic terminals in both targets ([20]their Fig. 5). Thus, convergent retrograde, molecular, and single-cell tract data point to the KF as a principal source of the EA calyces.

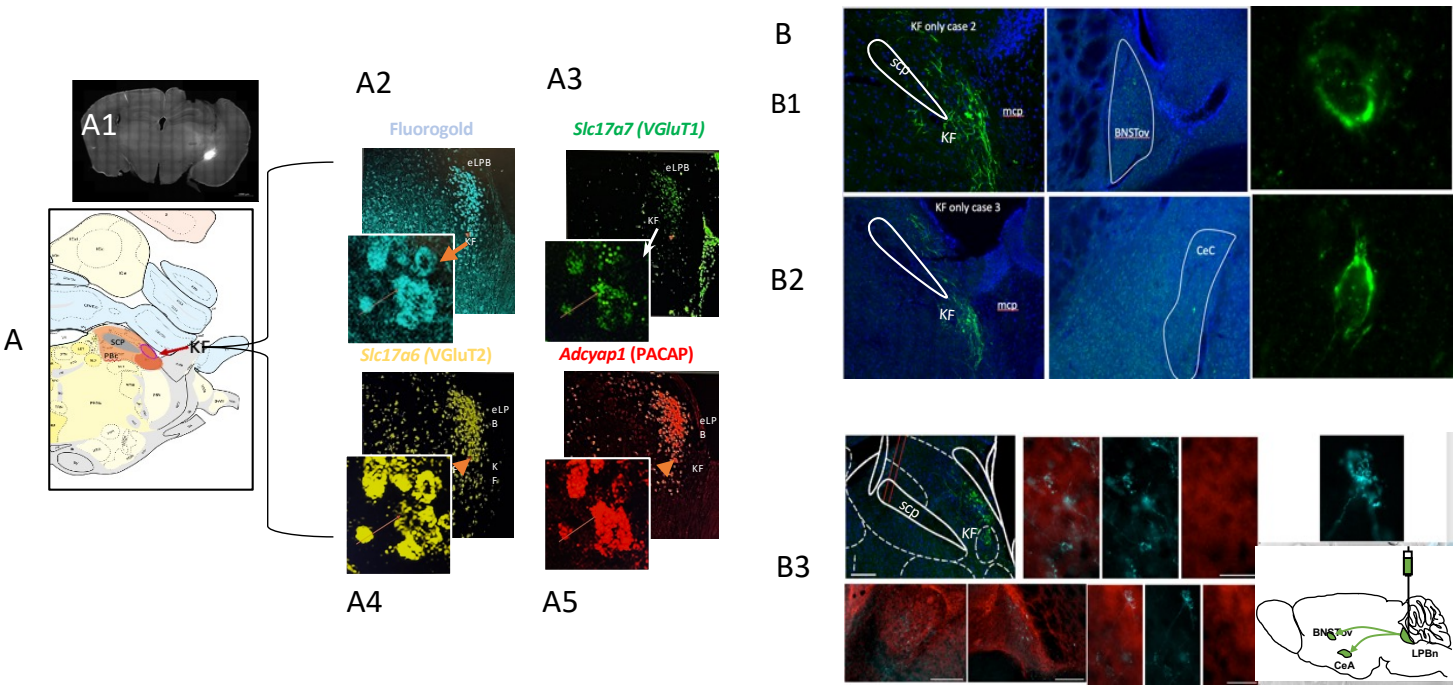

Figure 5. Pontine Kölliker–Fuse (KF) neurons give rise to calyx-like terminals in the extended amygdala. A, Retrograde and molecular identity (rat). Left, rat brain atlas schematics (Swanson, 2004; level 49) showing the KF within the ventrolateral parabrachial complex. A1, Fluoro-Gold (FG) was injected into CeC. A2–A5, in the KF, many FG-positive neurons co-expressed *Slc17a7* (VGluT1), *Slc17a6* (VGluT2), and *Adcyap1* (PACAP) mRNAs (insets with confocal microscope software general arrows indicating the same cells). This phenotype mirrors that of the EA calyceal terminals. B, Sufficiency test (mouse). **Highly restricted injections** of AAV5-EF1α-DIO-hChR2(H134R)-eYFP into PACAP-Cre mice yielded sparse labeling of PACAP$^+$ somata in KF (three successful cases). B1–B3, eYFP$^+$ axons formed ring-like perisomatic endings in BSTov (B1) and CeC (B2); in B3, rings are visible in both regions. Upper right panel in B1 shows a single axon giving two calyces in BSTov. Integration with prior single-cell anatomy. Consistent with these data, a juxtacellularly labeled KF neuron in rat projected scp to dorsal tegmental bundle to CeC to BSTov (ansa peduncularis) and formed calyceal-like perisomatic terminals in both EA targets ([20] Fig. 5), providing single-axon continuity from KF to CeC/BSTov. Abbreviations: BSTov, oval BNST; CeC, capsular central amygdala; eLPB, external lateral parabrachial subnucleus; FG, Fluoro-Gold; KF, Kölliker–Fuse; LPB, lateral parabrachial; PACAP, pituitary adenylate cyclase-activating polypeptide; scp, superior cerebellar peduncle.

Discussion

Giant axo-somatic synapses are exceedingly rare in the mammalian brain and, until now, have been confined to the auditory brainstem, where the calyx of Held ensures high-fidelity transmission required for precise sound localization [33, 34]. Here we identify a multimodal calyceal synapse in the extended amygdala (EA) - specifically in the capsular central amygdala

(CeC) and oval bed nucleus of the stria terminalis (BSTov) - revealed at the electron microscopic level through serial FIB-SEM reconstruction and correlated transmission immuno-electron microscopy. This forebrain calyx-like terminal, originating from PACAP-rich neurons in the pontine Kölliker–Fuse (KF) nucleus, represents a previously unrecognized anatomical substrate for rapid viscerosensory drive into limbic-autonomic circuits. Its giant, enveloping morphology, transmitter heterogeneity, and precise postsynaptic targeting distinguish it from all known cortical or limbic synapses. Complementing the anatomical definition here, a companion study shows that this KF PACAP/VGluT1 pathway is selectively engaged within 10 min of acute hypotension, preceding a delayed magnocellular SON/PVN activation, consistent with a fast autonomic limb followed by slower endocrine support [20].

Multimodal transmitter convergence in a single giant terminal. The KF-derived calyces co-express VGluT1/2 (glutamate), VAChT (acetylcholine), PACAP, CGRP, neurotensin, and calretinin, forming mixed type I and II synaptic specializations around their target somata. This represents an unprecedented level of transmitter convergence within one presynaptic element. In other brain regions, dual co-transmission (e.g., glutamate with ACh in habenular or basal forebrain neurons) supports temporal complementarity of fast ionotropic and slower metabotropic signaling [35, 36], but the combination of multiple peptides in a single axo-somatic terminal suggests a broader functional bandwidth - capable of coordinating immediate depolarization with longer-lasting excitability and plasticity modulation, consistent with the physiological role of the KF in mediating fast autonomic and arousal responses.

The coexistence of glutamatergic, cholinergic, and peptidergic markers within the same calyceal terminal illustrates the principle of neuronal co-transmission, where distinct transmitter classes are packaged in separate vesicle types and released depending on neuronal activity and intracellular calcium dynamics [37, 38]. This differential state-dependent release allows a single neuron to shift between rapid point-to-point excitation and slower modulatory actions that reconfigure circuit output and behavioral state. In this framework, the KF–extended amygdala calyx projection represents an extreme form of such multimodal signaling, combining high-fidelity glutamatergic and cholinergic excitation with PACAP and CGRP-mediated modulation. The structural integration of these systems likely allows to coordinate fast responses during transient sensory activation and prolonged modulation during sustained autonomic or emotional states.

GluD1 likely plays a roles beyond adhesion (notably, these GluD1-rich postsynaptic domains are the same neurons that show early Fos when hypotension is induced [20]). In the postsynaptic side, the calyces selectively target PKCδ^+ neurons that co-express GluD1, an atypical glutamate receptor originally considered a synaptic adhesion molecule [39, 40]. However, recent studies have redefined GluD1 as a metabotropic signal transduction device that couples to intracellular second messenger cascades and regulates synaptic organization and long-term potentiation [31, 32]. In our material, GluD1 immunogold particles were concentrated specifically at the symmetric (type II) synaptic contacts apposed to VAChT$^+$ presynaptic domains,

but were largely absent from the asymmetric, glutamatergic contacts within the same calyx (Fig. 4E). This highly selective distribution suggests that GluD1 participates in cholinergic and peptidergic synapse specialization, potentially coordinating postsynaptic responses to combined ACh/PACAP signaling. Through its intracellular signaling capacity, GluD1 may provide the postsynaptic PKCδ$^+$ neuron with a means to convert transient excitatory drive into longer-term adjustments of excitability, thus integrating fast and modulatory transmission in a single input channel.
Additionally it has been shown that glutamate delta receptors are functional glycine and serine gated cationic channels [41]. These aminoacids are classical gliotransmitters [42, 43], that have been shown to oscillate as a function of brain state and local neural activity [44, 45].

Recent work in the central amygdala has demonstrated that GluD1 signaling decreases excitatory input strength onto PKCδ$^+$ neurons and decrease averse and fear-learning behaviors[8]. In that system, cerebelin1 binding stabilizes GluD1-mediated synaptic organization, whereas D-serine shifts GluD1 toward a metabotropic signaling mode that engages intracellular cascades promoting neural excitation. By analogy, the cholinergic/peptidergic calyces described here may exploit this dual adhesive–metabotropic capacity of GluD1 to dynamically modulate synaptic efficacy in response to changes gliotransmitter tone. Such flexibility could provide a molecular substrate for state-dependent tuning of excitatory drive onto PKCδ$^+$ neurons, enabling multi-transmitter synapses to integrate fast, modulatory, and glial signals within a single structural unit.

A specialized Kölliker–Fuse subpopulation as the origin of forebrain calyces. Retrograde and anterograde tracing pinpointed the origin of these multimodal calyces to a discrete neuronal cohort in the Kölliker-Fuse subnucleus of the parabrachial complex, distinguished by co-expression of VGluT1, VGluT2, and PACAP mRNAs. The KF is a functionally heterogeneous structure involved in respiration, arousal, and cardiovascular regulation [46-48], but this particular subpopulation of PACAP/VGluT1/2$^+$ neurons is exceptionally well positioned to broadcast visceral state information to higher centers. The coexistence of glutamatergic and peptidergic machinery enables both rapid, time-locked excitation and slower, state-dependent modulation. Our combined viral tracing and FIB-SEM evidence demonstrates that these KF neurons generate the giant axo-somatic calyces in both CeC and BSTov, suggesting a unified pathway for high-fidelity transmission from the pons to limbic forebrain. The discovery of this KF lineage implies that calyceal synaptic precision is not restricted to the auditory pathway but can be redeployed in viscerosensory–emotional circuits. By broadcasting visceral state information through axo-somatic calyces, KF neurons may ensure that extended-amygdala ensembles receive temporally precise yet modulatable input, enabling rapid synchronization of defensive or homeostatic responses across CeC and BSTov.

Functional implications and circuit integration. Although our study is primarily anatomical, the structural organization of this ponto-limbic pathway offers an intuitive functional logic. The KF to EA calyx likely provides a high-gain, short-latency input capable of driving PKCδ$^+$ neurons

synchronously in response to visceral perturbations. [20] and aligns with the observed two-tier temporal sequence during hypotension - early KF to EA activation for sympathetic rebound and later SON/PVN recruitment for neurohormone mediated stabilization [20].

In turn, PKCδ$^+$ neurons in CeC and BSTov, known to be GABAergic and to project to preoptic and hypothalamic inhibitory relays, may exert disinhibitory control over presympathetic neurons in the paraventricular nucleus (PVN) [27, 49]. This arrangement would allow rapid reactivation of sympathetic tone during acute hypotension, preceding slower hormonal responses. Consistent with this interpretation, prior work [13] demonstrated early Fos activation in lateral/central amygdala neurons following hydralazine-induced hypotension, well before magnocellular AVP neurons were engaged. The KF to CeC/BSTov calyceal pathway thus provides a plausible anatomical substrate for this early phase of autonomic recovery, that complements slower endocrine and behavioral components of the response to hypotension. Comparable parabrachial-amygdalar channels have been implicated in transmitting interoceptive and autonomic information [16, 50], but the calyceal specialization identified here introduces a synaptic mechanism for near-instantaneous synchronization of these signals. Thus, KF-driven calyceal excitation of PKCδ/GluD1 neurons provides a plausible forebrain route to re-engage RVLM-centered sympathetic premotor circuits during the "autonomic rescue" window documented in the hydralazine model [20].

By uncovering a multimodal calyx-like synapse in the forebrain, this study broadens the known repertoire of mammalian synaptic architectures and demonstrates that calyceal precision is not exclusive to sensory processing. The structural integration of glutamatergic, cholinergic, and peptidergic signaling within a single giant synapse suggests a mechanism by which the forebrain can couple rapid neural responses to modulatory context, uniting visceral feedback with emotional and homeostatic regulation. Future work should examine whether similar multimodal calyces exist in other limbic or hypothalamic regions and explore how GluD1-mediated signaling contributes to their function and plasticity. Together, these findings redefine the extended amygdala as a high-fidelity viscerosensory hub and establish a new anatomical framework for understanding how the brainstem orchestrates emotional and autonomic integration at the cellular level.

References

1. Nakamura, P.A. and K.S. Cramer, *Formation and maturation of the calyx of Held.* Hear Res, 2011. **276**(1-2): p. 70–8.
2. Held, H., *Die centrale Gehörleitung.* Arch Anat Physiol Anat Abt,, 1893.
3. Satzler, K., et al., *Three-dimensional reconstruction of a calyx of Held and its postsynaptic principal neuron in the medial nucleus of the trapezoid body.* J Neurosci, 2002. **22**(24): p. 10567–79.
4. Lorteije, J.A., et al., *Reliability and precision of the mouse calyx of Held synapse.* J Neurosci, 2009. **29**(44): p. 13770–84.

5. Schneggenburger, R. and I.D. Forsythe, *The calyx of Held.* Cell Tissue Res, 2006. **326**(2): p. 311–37.
6. Harris, K.M. and R.J. Weinberg, *Ultrastructure of synapses in the mammalian brain.* Cold Spring Harb Perspect Biol, 2012. **4**(5).
7. Schwaber, J.S., et al., *Neurons containing calcitonin gene-related peptide in the parabrachial nucleus project to the central nucleus of the amygdala.* J Comp Neurol, 1988. **270**(3): p. 416–26, 398–9.
8. Gandhi, P.J., et al., *Dysfunction of Glutamate Delta-1 Receptor-Cerebellin 1 Trans-Synaptic Signaling in the Central Amygdala in Chronic Pain.* Cells, 2021. **10**(10).
9. Shimada, S., et al., *Calcitonin gene-related peptidergic projection from the parabrachial area to the forebrain and diencephalon in the rat: an immunohistochemical analysis.* Neuroscience, 1985. **16**(3): p. 607–16.
10. Dong, Y.L., et al., *Differential postsynaptic compartments in the laterocapsular division of the central nucleus of amygdala for afferents from the parabrachial nucleus and the basolateral nucleus in the rat.* J Comp Neurol, 2010. **518**(23): p. 4771–91.
11. Missig, G., et al., *Parabrachial nucleus (PBn) pituitary adenylate cyclase activating polypeptide (PACAP) signaling in the amygdala: implication for the sensory and behavioral effects of pain.* Neuropharmacology, 2014. **86**: p. 38–48.
12. Torruella-Suarez, M.L., et al., *Manipulations of Central Amygdala Neurotensin Neurons Alter the Consumption of Ethanol and Sweet Fluids in Mice.* J Neurosci, 2020. **40**(3): p. 632–647.
13. Takeuchi, Y., et al., *Parabrachial inputs to Fos-immunoreactive neurons in the lateral central nucleus of amygdala activated by hypotension: a light and electron microscopic study in the rat.* Brain Res Bull, 2004. **64**(2): p. 171–80.
14. Goehler, L., *Vicerosensory pathway in the brain*, in *The science and clinical application of manual therapy*, H. King, J. W, and M. Patterson, Editors. 2011, Churchill Livingston Elsevier: Edinburgh. p. 163–179.
15. Crestani, C.C., et al., *Mechanisms in the bed nucleus of the stria terminalis involved in control of autonomic and neuroendocrine functions: a review.* Curr Neuropharmacol, 2013. **11**(2): p. 141–59.
16. Jaramillo, A.A., J.A. Brown, and D.G. Winder, *Danger and distress: Parabrachial-extended amygdala circuits.* Neuropharmacology, 2021. **198**: p. 108757.
17. Jiang, S.Z., H.Y. Zhang, and L.E. Eiden, *PACAP Controls Endocrine and Behavioral Stress Responses via Separate Brain Circuits.* Biol Psychiatry Glob Open Sci, 2023. **3**(4): p. 673–685.
18. Radke, A.K., *The role of the bed nucleus of the stria terminalis in learning to fear.* J Neurosci, 2009. **29**(49): p. 15351–2.
19. Daniel, S.E. and D.G. Rainnie, *Stress Modulation of Opposing Circuits in the Bed Nucleus of the Stria Terminalis.* Neuropsychopharmacology, 2016. **41**(1): p. 103–25.
20. Botta, P., et al., *Regulating anxiety with extrasynaptic inhibition.* Nat Neurosci, 2015. **18**(10): p. 1493–500.
21. Takacs, V.T., T.F. Freund, and G. Nyiri, *Neuroligin 2 is expressed in synapses established by cholinergic cells in the mouse brain.* PLoS One, 2013. **8**(9): p. e72450.
22. Wainer, B.H., et al., *Cholinergic synapses in the rat brain: a correlated light and electron microscopic immunohistochemical study employing a monoclonal antibody against choline acetyltransferase.* Brain Res, 1984. **308**(1): p. 69–76.
23. Dai, J., et al., *GluD1 is a signal transduction device disguised as an ionotropic receptor.* Nature, 2021. **595**(7866): p. 261–265.

24. Liakath-Ali, K., et al., *Transsynaptic cerebellin 4-neogenin 1 signaling mediates LTP in the mouse dentate gyrus.* Proc Natl Acad Sci U S A, 2022. **119**(20): p. e2123421119.
25. Weihe, E., et al., *Visualization of the vesicular acetylcholine transporter in cholinergic nerve terminals and its targeting to a specific population of small synaptic vesicles.* Proc Natl Acad Sci U S A, 1996. **93**(8): p. 3547–52.

Materials and methods

Adult (>60 days) male Wistar rats were obtained from the vivarium of the School of Medicine, National Autonomous University of Mexico. Rats were housed under controlled temperature and humidity on a 12-h light cycle (lights on at 07:00, off at 19:00) with ad libitum access to standard chow and water. All procedures were approved by the School of Medicine's Ethics Committee (License: CIEFM-079-2020).

PKCδ-Ai9-TdTomato mice were generated by crossing heterozygous Prkcd-Cre knock-in mice (Jackson Laboratory, stock #027857) with Ai9 Cre-dependent reporter mice (stock #007909); double-positive offspring were identified via PCR. In addition, adult male and female C57BL/6J wild-type and PKCδ-Ai9 animals were maintained under similar conditions. All procedures with mice were approved by the National Institute of Mental Health Animal Care and Use Committee (NIMH/ACUC approval LCMR-08).

Immunohistochemistry for light microscopy. Rodents were perfused via the ascending aorta with 0.9% NaCl followed by 4% paraformaldehyde. Brains were sectioned at 70 µm using a Leica VT1200 vibratome. Sections were washed in phosphate buffer (PB), blocked for 2 hours in TBST (0.05 M Tris, 0.9% NaCl, 0.3% Triton-X) plus 10% normal donkey serum, and incubated overnight at 4°C with primary antibodies (see SI table 1 diluted in TBST with 1% serum. After washing, sections were incubated for 2 hours at room temperature with appropriate biotinylated or fluorescent secondary antibodies (1:500; Vector Laboratories). Brightfield images were acquired using a Nikon Eclipse E600, and confocal images were acquired with a Leica Stellaris microscope.

RNAscope: Brains were rapidly dissected, flash-frozen on dry ice, and stored at −80 °C until sectioning. Coronal sections (16 µm) were cut at −20 °C and mounted onto slides, which were stored at −80 °C until use. RNAscope in situ hybridization was performed following manufacturer instructions (Advanced Cell Diagnostics) and published protocols. Briefly, slides were fixed in 10% neutral buffered formalin for 20 min at 4 °C, washed in PBS, and dehydrated through graded ethanol (50%, 70%, 100%; 5 min each). After overnight storage in 100% ethanol at −20 °C, slides were air-dried and circled with a PAP pen. Sections were treated with Protease IV for 20 min at room temperature, rinsed, and hybridized with probes for 2 h at 40 °C in a HybEZ™ oven. The following probes were used: Mm-Grid1-C1 (Cat. 552311), Mm-Adcyap1r1-C2 (Cat. 409561-C2), Mm-Chrna7-C3 (Cat. 465161-C3) and Mm-Sst-C3 (Cat No. 404631-C3). After hybridization, slides were washed, processed through the amplification steps, counterstained with DAPI, and coverslipped. Images were acquired with a Leica Stellaris confocal microscope using a 20× objective and DAPI, Alexa Fluor 488, 550, and 647 channels.

***Ex vivo* whole-cell electrophysiology**. Brain slices (300 μm thick) containing the central amygdala (CeA) were obtained from Ai9-TdTomato-PKCδ mice. Following rapid extraction, brains were placed in an ice-cold cutting solution (in mM: 92 NMDG, 20 HEPES, 25 glucose, 30 $NaHCO_3$, 2.5 KCl, 1.2 NaH_2PO_4, 10 $MgSO_4$, 0.5 $CaCl_2$; osmolarity 303–306 mOsm; 95% O_2/5% CO_2). Slices were cut with a Leica VT1200 and incubated at 34°C for 5 minutes, then maintained in holding aCSF (in mM: 92 NaCl, 20 HEPES, 25 glucose, 30 $NaHCO_3$, 2.5 KCl, 1.2 NaH_2PO_4, 1 $MgSO_4$, 2 $CaCl_2$) at room temperature for at least 1 hour. For current-clamp recordings, micropipettes (3–5 MΩ) were filled with an internal solution (in mM: 135 K-gluconate, 10 HEPES, 4 KCl, 4 Mg-ATP, 0.3 Na-GTP, 0.2% biocytin). Neurons were visualized using differential interference contrast (DIC) and identified by TdTomato fluorescence. PACAP (100 nM) was bath-applied during a current injection protocol (1 s steps from -40 to 240 pA in 20 pA increments, 7 s intervals), and data were analyzed using GraphPad Prism. Only cells with stable series resistance (<20 MΩ) were included.

Transmission Electron Microscopy. Brains from C57BL/6 mice were sectioned at 40 μm (Leica VT1000) and processed for immuno-EM. Sections were rinsed in PB, incubated in 1% sodium borohydride for 30 minutes, and blocked in a solution containing 1% normal goat serum and 4% bovine serum albumin in PB with 0.02% saponin. Primary antibodies (see SI table 1) were applied for 24 h at 4°C in blocking solution. After rinsing, sections were incubated overnight at 4°C with Nanogold-Fab' secondary antibodies (1:100) and processed using Vectastain ABC-HRP kits. Silver enhancement was performed with the HQ Silver Enhancement Kit (7 min at room temperature), followed by visualization of DAB reaction (0.025% DAB, 0.003% H_2O_2). Sections were post-fixed with 0.5% osmium tetroxide, stained with uranyl acetate, dehydrated through graded ethanol and propylene oxide, and flat embedded in Durcupan ACM epoxy resin. Ultrathin sections (~60 nm) were cut using a Leica Ultramicrotome UC7, collected on formvar-coated grids, counterstained with Reynolds lead citrate, and imaged using a Tecnai G2 12 transmission electron microscope with a OneView digital camera.

FIB-SEM Tomography. For three-dimensional reconstruction of calyx-like contacts at electron microscopical level, slices previously processed for PACAP immunolabeling were embedded in Durcupan resin and platinum-coated. A ZEISS Crossbeam 550 FIB-SEM was used. After milling a coarse trench with a 15 nA ion beam, a protective platinum layer (~1 μm thick) was deposited using the gas injection system at 30 kV/3 nA. A chevron-patterned registration mark was milled for alignment. Serial backscattered electron images were acquired using an accelerating voltage of 3 kV and a pixel size of 20 nm × 10 nm, with a slice thickness of 20 nm. The image stack was assembled into a volume and analyzed using ORS Dragonfly software.

Blood Pressure Measurements. The blood pressure (BP) measurements in conscious rats were done between 10:00 a.m. and 03:00 p.m. via a non-invasive tail-cuff CODA system (Kent Scientific Corp., USA). Animals were acclimated to restraining device and the sensing tail-cuff during 30 min to avoid unnecessary stress in the course of measurements. During recording, the occlusion cuff and the volume pressure recording (VPR) sensor was positioned on the tail base while the rats were maintained in a heater platform set to 30 °C to induce vasodilation, which enhances the blood flow to the tail. Data of

BP (the average of 3 times) were evaluated two times at basal level and 5, 10, 15, 30 and 60, 90 and 120 minutes after hydralazine (10 mg/Kg-1) or saline (0.9 % NaCl, 1 mL/Kg-1) intraperitoneal administration. CODA software displays the systolic, diastolic and mean blood pressure data in mmHg units. Data are expressed as mean ± SEM of BP measurements in mmHg of at least 3 rats per condition and indicated time. Statistical analysis was performed using two-way ANOVA followed by Fisher's LSD multiple comparisons post hoc test, a statistically significant difference was set with a P value < 0.05.

Statistics. Data from electrophysiological recordings were analyzed by classifying neurons as PACAP responders (n = 21) or non-responders (n = 9) using a two-way ANOVA with treatment (baseline, PACAP, washout) and current step amplitude as factors. GraphPad Prism was used for statistical comparisons.

See supplemental Information (SI) for details of materials and method and a summary of primary and secondary antibodies, including dilutions, sources, and catalog numbers, in the SI Table 1.

Acknowledgements

This research was supported by funding from the following sources: the National Autonomous University of Mexico (UNAM-PAPIIT-IG200121 to LZ and RAB); the Mexican Secretaría de Ciencia, Humanidad, Tecnología e Innovación (Secihti, CF-2023-G-243 to LZ, RAB, and RHP; CB-238744 to RAB); and the Intramural Research Program of the NIMH, NIH (ZIAMH002386 to LEE). The investigators were additionally supported by fellowships, including: a sabbatical year fellowship from the PASPA-DGAPA program (UNAM, to LZ and VSH); a Secihti sabbatical fellowship (to LZ); and a Fulbright-García Robles Fellowship (to VSH). We extend our deepest gratitude to Rafael Luján (UCLM, Spain), Luis Miguel García-Segura, Javier deFelipe, and Angel Merchán (Cajal Institute, Spain), Sebastian Schädler (Carl Zeiss Microscopy GmbH, Germany), and Claus Burkhart (NMI, Germany) for their invaluable guidance and support in FIB-SEM techniques. We thank Marisela Morales for introducing us to the NIDA Confocal and Electron Microscopy Core and Pedro Segura for technical assistance. Finally, LZ wishes to express her profound gratitude to her mentor, Peter Somogyi, for hosting her 2019 summer research stay in Oxford, for his time spent examining raw materials under the microscope together with her, and for his insightful suggestion regarding the possibility of a Calyx of Held-like synapse.

References

1. Nakamura, P.A. and K.S. Cramer, *Formation and maturation of the calyx of Held.* Hear Res, 2011. **276**(1-2): p. 70–8.
2. Held, H., *Die centrale Gehörleitung.* Arch Anat Physiol Anat Abt,, 1893.
3. Satzler, K., et al., *Three-dimensional reconstruction of a calyx of Held and its postsynaptic principal neuron in the medial nucleus of the trapezoid body.* J Neurosci, 2002. **22**(24): p. 10567–79.
4. Lorteije, J.A., et al., *Reliability and precision of the mouse calyx of Held synapse.* J Neurosci, 2009. **29**(44): p. 13770–84.
5. Schneggenburger, R. and I.D. Forsythe, *The calyx of Held.* Cell Tissue Res, 2006. **326**(2): p. 311–37.

6. Harris, K.M. and R.J. Weinberg, *Ultrastructure of synapses in the mammalian brain.* Cold Spring Harb Perspect Biol, 2012. **4**(5).
7. Schwaber, J.S., et al., *Neurons containing calcitonin gene-related peptide in the parabrachial nucleus project to the central nucleus of the amygdala.* J Comp Neurol, 1988. **270**(3): p. 416–26, 398–9.
8. Gandhi, P.J., et al., *Dysfunction of Glutamate Delta-1 Receptor-Cerebellin 1 Trans-Synaptic Signaling in the Central Amygdala in Chronic Pain.* Cells, 2021. **10**(10).
9. Shimada, S., et al., *Calcitonin gene-related peptidergic projection from the parabrachial area to the forebrain and diencephalon in the rat: an immunohistochemical analysis.* Neuroscience, 1985. **16**(3): p. 607–16.
10. Dong, Y.L., et al., *Differential postsynaptic compartments in the laterocapsular division of the central nucleus of amygdala for afferents from the parabrachial nucleus and the basolateral nucleus in the rat.* J Comp Neurol, 2010. **518**(23): p. 4771–91.
11. Missig, G., et al., *Parabrachial nucleus (PBn) pituitary adenylate cyclase activating polypeptide (PACAP) signaling in the amygdala: implication for the sensory and behavioral effects of pain.* Neuropharmacology, 2014. **86**: p. 38–48.
12. Torruella-Suarez, M.L., et al., *Manipulations of Central Amygdala Neurotensin Neurons Alter the Consumption of Ethanol and Sweet Fluids in Mice.* J Neurosci, 2020. **40**(3): p. 632–647.
13. Takeuchi, Y., et al., *Parabrachial inputs to Fos-immunoreactive neurons in the lateral central nucleus of amygdala activated by hypotension: a light and electron microscopic study in the rat.* Brain Res Bull, 2004. **64**(2): p. 171–80.
14. Goehler, L., *Vicerosensory pathway in the brain*, in *The science and clinical application of manual therapy*, H. King, J. W, and M. Patterson, Editors. 2011, Churchill Livingston Elsevier: Edinburgh. p. 163–179.
15. Crestani, C.C., et al., *Mechanisms in the bed nucleus of the stria terminalis involved in control of autonomic and neuroendocrine functions: a review.* Curr Neuropharmacol, 2013. **11**(2): p. 141–59.
16. Jaramillo, A.A., J.A. Brown, and D.G. Winder, *Danger and distress: Parabrachial-extended amygdala circuits.* Neuropharmacology, 2021. **198**: p. 108757.
17. Jiang, S.Z., H.Y. Zhang, and L.E. Eiden, *PACAP Controls Endocrine and Behavioral Stress Responses via Separate Brain Circuits.* Biol Psychiatry Glob Open Sci, 2023. **3**(4): p. 673–685.
18. Haubensak, W., et al., *Genetic dissection of an amygdala microcircuit that gates conditioned fear.* Nature, 2010. **468**(7321): p. 270–6.
19. Herman, J.P., et al., *Local circuit regulation of paraventricular nucleus stress integration: glutamate-GABA connections.* Pharmacol Biochem Behav, 2002. **71**(3): p. 457–68.
20. Hernandez, V.S., P.D. Segura-Chama, and L. Zhang, *KF/parabrachial complex PACAP - glutamate pathway to the extended amygdala couples rapid autonomic and delayed endocrine responses to acute hypotension.* bioRxiv, 2025: p. 2025.10.16.682741.
21. Saper, C.B. and A.D. Loewy, *Efferent connections of the parabrachial nucleus in the rat.* Brain Res, 1980. **197**(2): p. 291–317.
22. Jhamandas, J.H., et al., *Parabrachial nucleus projection to the amygdala in the rat: electrophysiological and anatomical observations.* Brain Res Bull, 1996. **39**(2): p. 115–26.
23. Gauriau, C. and J.F. Bernard, *Pain pathways and parabrachial circuits in the rat.* Exp Physiol, 2002. **87**(2): p. 251–8.
24. Bernard, J.F., M. Alden, and J.M. Besson, *The organization of the efferent projections from the pontine parabrachial area to the amygdaloid complex: a Phaseolus vulgaris leucoagglutinin (PHA-L) study in the rat.* J Comp Neurol, 1993. **329**(2): p. 201–29.

25. Chiang, M.C., et al., *Parabrachial Complex: A Hub for Pain and Aversion.* J Neurosci, 2019. **39**(42): p. 8225–8230.
26. Geerling, J.C., et al., *Kolliker-Fuse GABAergic and glutamatergic neurons project to distinct targets.* J Comp Neurol, 2017. **525**(8): p. 1844–1860.
27. Daniel, S.E. and D.G. Rainnie, *Stress Modulation of Opposing Circuits in the Bed Nucleus of the Stria Terminalis.* Neuropsychopharmacology, 2016. **41**(1): p. 103–25.
28. Botta, P., et al., *Regulating anxiety with extrasynaptic inhibition.* Nat Neurosci, 2015. **18**(10): p. 1493–500.
29. Takacs, V.T., T.F. Freund, and G. Nyiri, *Neuroligin 2 is expressed in synapses established by cholinergic cells in the mouse brain.* PLoS One, 2013. **8**(9): p. e72450.
30. Wainer, B.H., et al., *Cholinergic synapses in the rat brain: a correlated light and electron microscopic immunohistochemical study employing a monoclonal antibody against choline acetyltransferase.* Brain Res, 1984. **308**(1): p. 69–76.
31. Dai, J., et al., *GluD1 is a signal transduction device disguised as an ionotropic receptor.* Nature, 2021. **595**(7866): p. 261–265.
32. Liakath-Ali, K., et al., *Transsynaptic cerebellin 4-neogenin 1 signaling mediates LTP in the mouse dentate gyrus.* Proc Natl Acad Sci U S A, 2022. **119**(20): p. e2123421119.
33. Nakakubo, Y., et al., *Vesicular Glutamate Transporter Expression Ensures High-Fidelity Synaptic Transmission at the Calyx of Held Synapses.* Cell Rep, 2020. **32**(7): p. 108040.
34. Baydyuk, M., J. Xu, and L.G. Wu, *The calyx of Held in the auditory system: Structure, function, and development.* Hear Res, 2016. **338**: p. 22–31.
35. Frahm, S., et al., *An essential role of acetylcholine-glutamate synergy at habenular synapses in nicotine dependence.* Elife, 2015. **4**: p. e11396.
36. Granger, A.J., et al., *Cotransmission of acetylcholine and GABA.* Neuropharmacology, 2016. **100**: p. 40–6.
37. Svensson, E., et al., *General Principles of Neuronal Co-transmission: Insights From Multiple Model Systems.* Front Neural Circuits, 2018. **12**: p. 117.
38. Nusbaum, M.P., D.M. Blitz, and E. Marder, *Functional consequences of neuropeptide and small-molecule co-transmission.* Nat Rev Neurosci, 2017. **18**(7): p. 389–403.
39. Ryu, K., et al., *Induction of excitatory and inhibitory presynaptic differentiation by GluD1.* Biochem Biophys Res Commun, 2012. **417**(1): p. 157–61.
40. Tao, W., et al., *Postsynaptic delta1 glutamate receptor assembles and maintains hippocampal synapses via Cbln2 and neurexin.* Proc Natl Acad Sci U S A, 2018. **115**(23): p. E5373–E5381.
41. Carrillo, E., et al., *Delta glutamate receptors are functional glycine- and D-serine-gated cation channels in situ.* Sci Adv, 2021. **7**(52): p. eabk2200.
42. Bardoczi, Z., et al., *Glycinergic Input to the Mouse Basal Forebrain Cholinergic Neurons.* J Neurosci, 2017. **37**(39): p. 9534–9549.
43. Abreu, D.S., et al., *Astrocytes control hippocampal synaptic plasticity through the vesicular-dependent release of D-serine.* Front Cell Neurosci, 2023. **17**: p. 1282841.
44. Miller, R.F., *D-Serine as a glial modulator of nerve cells.* Glia, 2004. **47**(3): p. 275–283.
45. Papouin, T., et al., *Septal Cholinergic Neuromodulation Tunes the Astrocyte-Dependent Gating of Hippocampal NMDA Receptors to Wakefulness.* Neuron, 2017. **94**(4): p. 840–854 e7.
46. Benarroch, E.E., *Brainstem integration of arousal, sleep, cardiovascular, and respiratory control.* Neurology, 2018. **91**(21): p. 958–966.
47. Krohn, F., et al., *The integrated brain network that controls respiration.* Elife, 2023. **12**.

48. Moreira, T.S., et al., *Neuroanatomical and neurochemical organization of brainstem and forebrain circuits involved in breathing regulation.* J Neurophysiol, 2025. **133**(4): p. 1116–1137.
49. Tsubouchi, K., et al., *A disynaptic pathway from the central amygdaloid nucleus to the paraventricular hypothalamic nucleus via the parastrial nucleus in the rat.* Neurosci Res, 2007. **59**(4): p. 390–8.
50. Bernard, J.F., H. Bester, and J.M. Besson, *Involvement of the spino-parabrachio -amygdaloid and -hypothalamic pathways in the autonomic and affective emotional aspects of pain.* Prog Brain Res, 1996. **107**: p. 243–55.
51. Weihe, E., et al., *Visualization of the vesicular acetylcholine transporter in cholinergic nerve terminals and its targeting to a specific population of small synaptic vesicles.* Proc Natl Acad Sci U S A, 1996. **93**(8): p. 3547–52.

Supplemental information

Multimodal calyx-like synapse in the extended amygdala drives fast visceral control from the hindbrain

Limei Zhang[1, 2†,10*], Vito S. Hernández[1, 2†,10], David M. Giraldo[3, 4], Sunny Z. Jiang[2], Juan C. León-Contreras[5], Rong Ye[6], Shiliang Zhang[6], Martin K-H Schäfer[7], Pedro D. Segura-Chama[1], Rafael A. Barrio[8], Rogelio Hernández-Pando[5], Sabine Schoenherr[9], Francesco Ferraguti[9], and Lee E. Eiden[2]

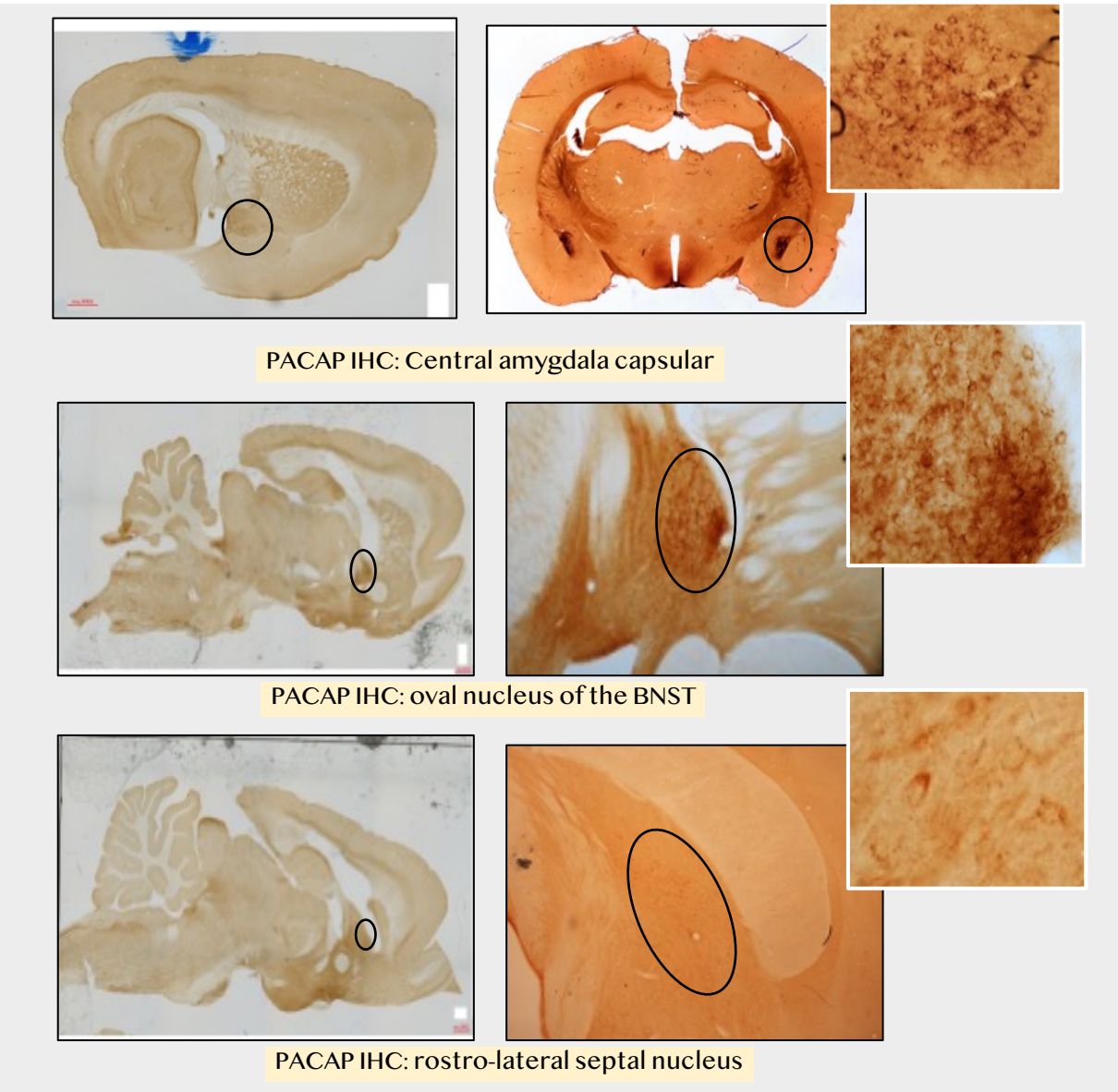

SI –Figure 1. Calyceal axonal endings in male adult rats telencephalic structures observed with PACAP immunohistochemistry. Upper raw, central amygdala, capsular subdivision (CeC). Inset is taken from a sagittal section. Meddle raw: oval nucleus of the bed nucleus of the stria terminalis (BSTov). Bottom raw: rostro-lateral septal nucleus.

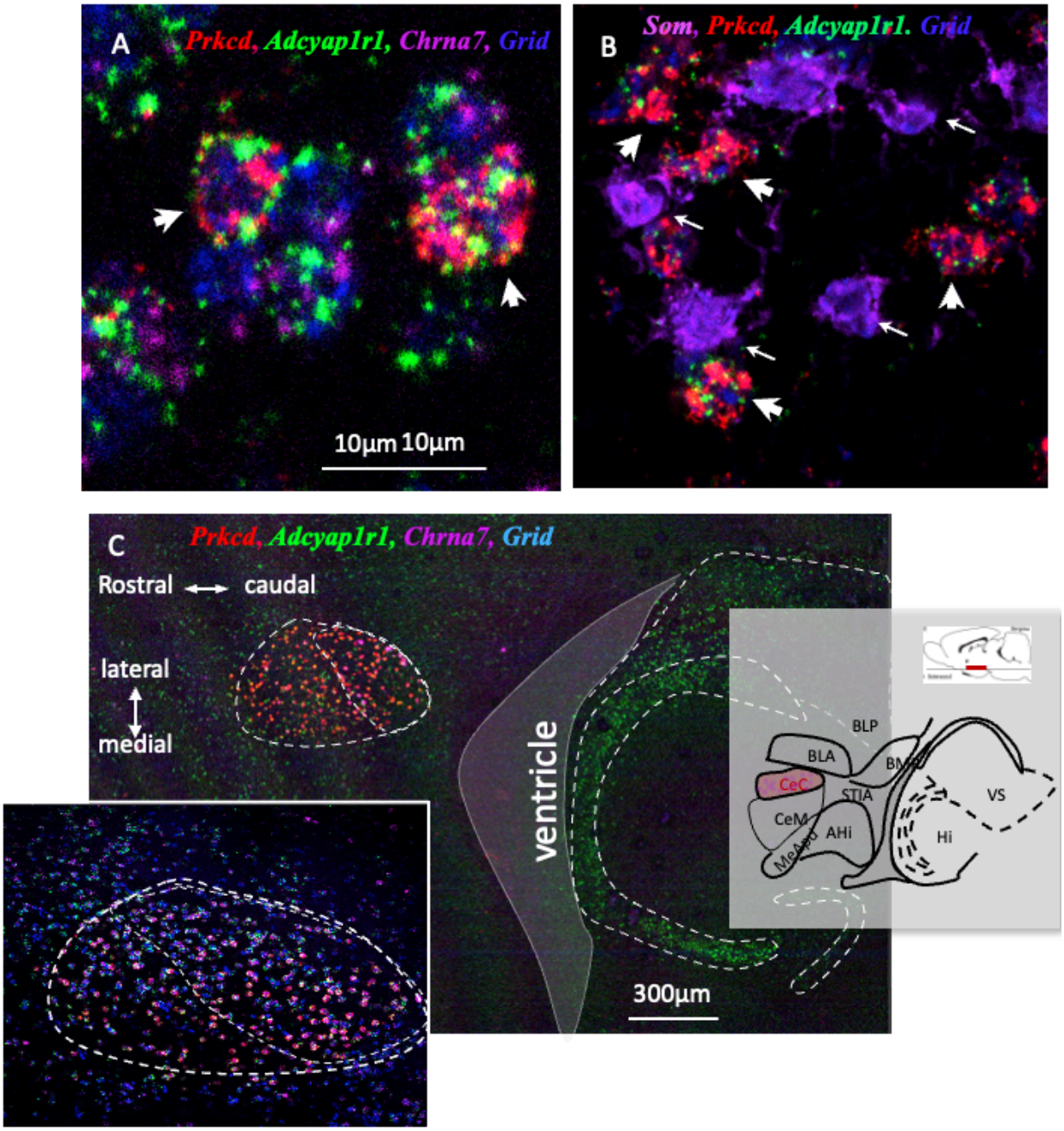

SI –Figure 2. Molecular signature of the calyceal synapse target PKCd+ cells in CeC PKCd cells. A: *Prkcd* cells co-expressing *Adcyap1r1* (PAC1,) *Grid1* (GluD1), *Chrna7* (nAChRa7) (thick arrows); (B) while *Som* (somatostatin) expressing neurons do not co-express *Adcyapr1r* nor *Prkcd* (B, thin white arrows). Panel C is a horizontal section showing the the selective distribution, in the ventral posterior segment of the CeC, of the population co-expressing PKCd + cells (Prkcd cells) co-expressing Adcyap1r1 (PAC1,) Grid1 (GluD1), Chrna7 (nAChRa7).

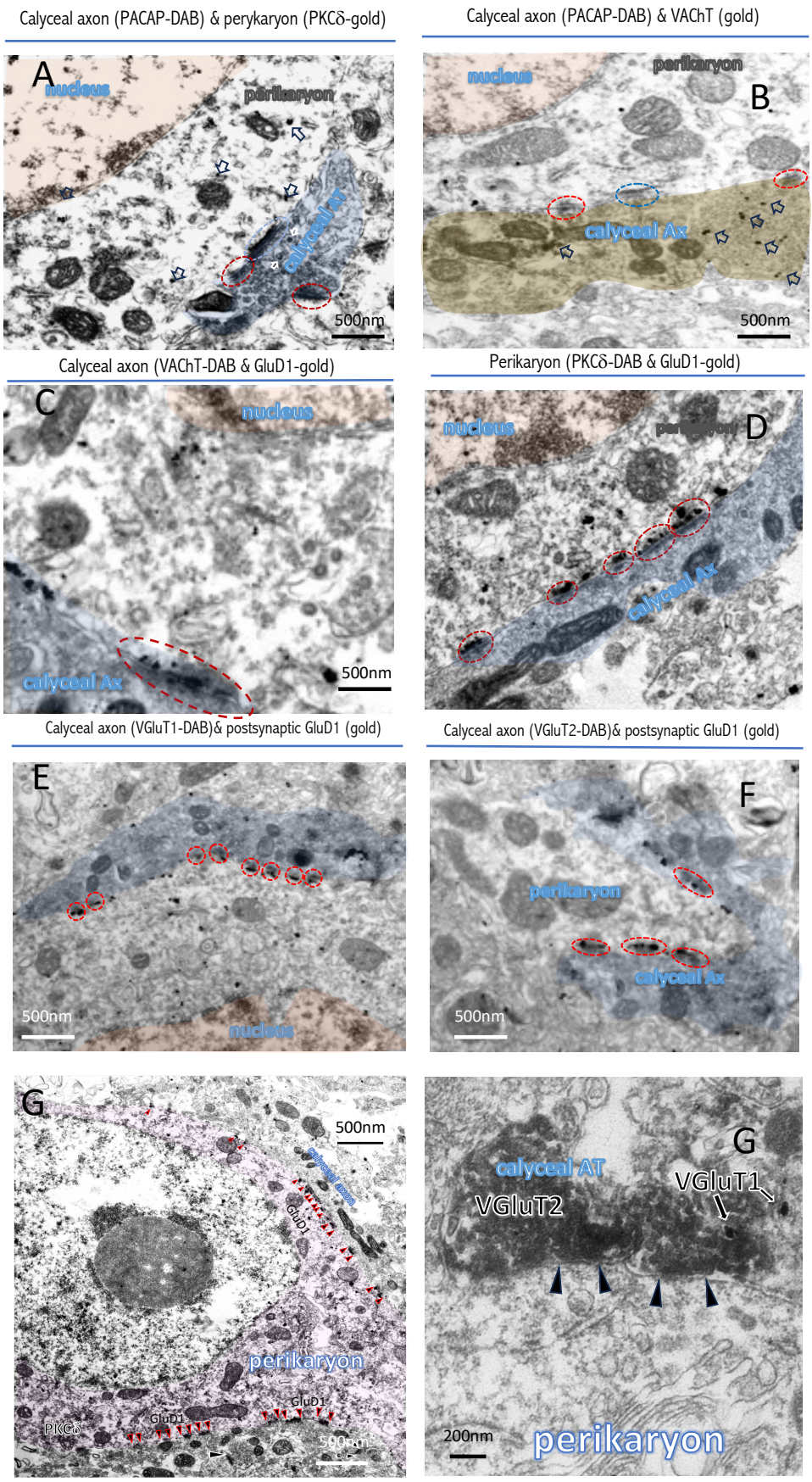

SI Figure 3. Dual immunoelectron microcopy micrographs showing main ultrastructural features of the calyceal synapse. A. A PACAP-ir calyceal axon (DAB) making type 1 (blue circle) and type 2 (red circle) synapses onto a PKCd labeled soma (gold particle). B. co-expression of PACAP (DAB) and VAhT (gold particle) of a calyceal axon (DAB) making type 1 (blue circle) and type 2 (red circle) synapses onto a soma. C. A VAChT-ir calyceal axon (DAB) making type 2 (red circle) on to a soma with numerous GluD1-gold particles located at the postsynaptic density (PSD). D. Perikaryon with PKCd-DAB & GluD1-gold labeling. E. A VGluT1-ir calyceal axon (DAB) with numerous GluD1-gold particles labeled synaptic specifications. F. A VGluT2-ir calyceal axon (DAB) with numerous GluD1-gold particles labeled synaptic specifications. G. A large PKCδ-expressing (DAB-labeled) neuron receives multiple GluD1-positive synaptic contacts (red-black arrowheads) along its soma and proximal dendrite. Two adjacent type I synapses from unlabeled axons are GluD1-negative (white-black arrowheads), underscoring the specificity of GluD1 labeling to type II synapses and suggesting a molecular distinction between glutamatergic and cholinergic inputs. G. VGluT1+/2+ axon terminal. Arrowhead indicate synaptic specifications.

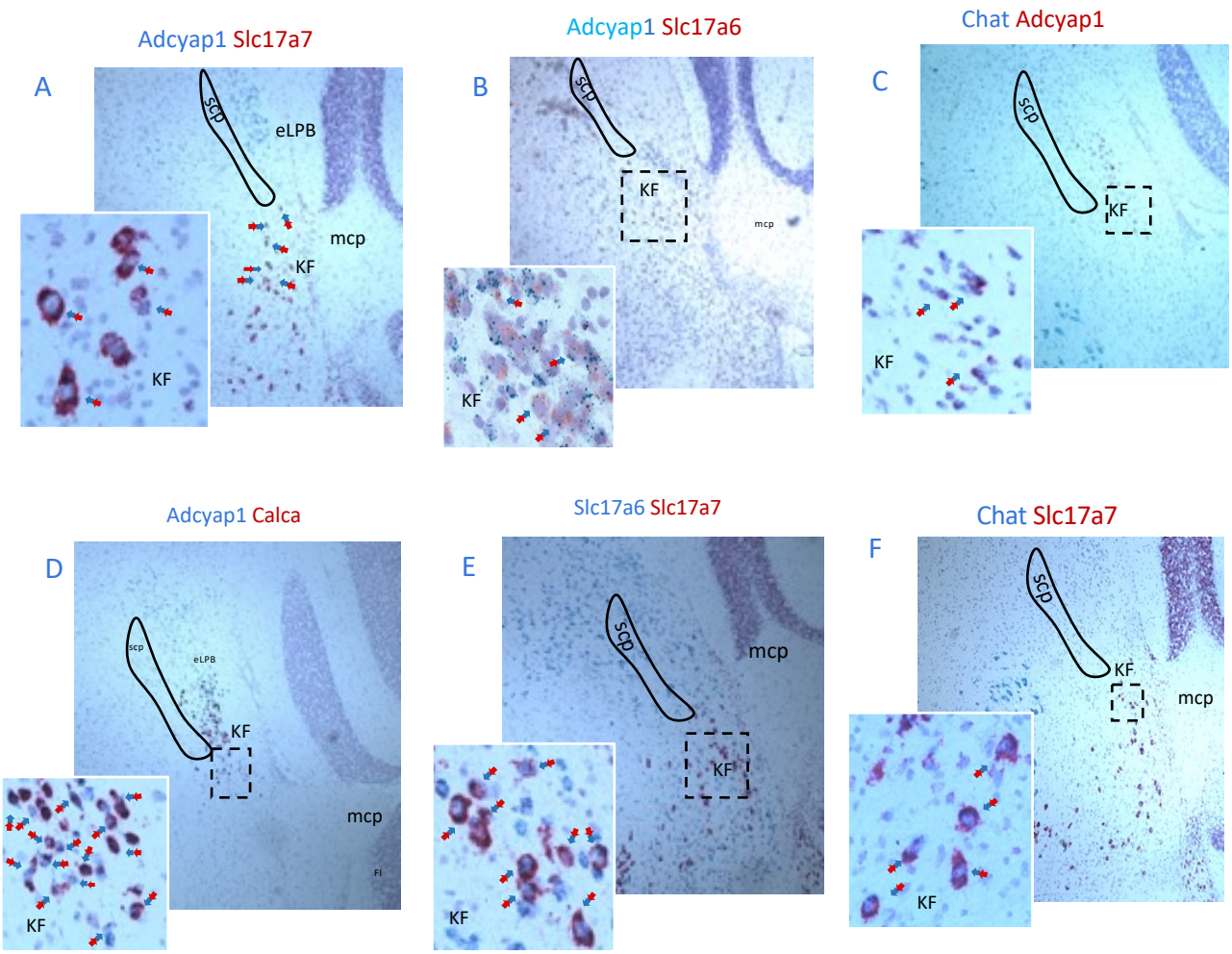

SI Figure 4: Dual *in situ* hybridization (DISH) revealed the "large cells" in the Kölliker-Fuse area co-expressed mRNAs A) Adcyap1 (PACAP) with Slc17a7 (VGLUT1), B) Adcyap1 (PACAP) with Slc17a6 (VGLUT2); C) Adcyap1 (PACAP) with Chat (CHAT); D) Adcyap1 (PACAP) with Calca (CGRP); E) Slc17a6 (VGluT1) with Slc17a7 (VGluT2); F) Chat (CHAT) with Slc17a7 (VGluT1).

Extended Materials and methods

Animals

Rats: Adult (>60 days) male Wistar rats were obtained from the vivarium of the School of Medicine of the National Autonomous University of Mexico. Rats were housed in humidity and temperature-controlled vivarium using a normal light cycle with lights on at 7:00 hours and lights off at 19:00 hours. Animals had *ad-libitum* access to standard laboratory chow and water. All procedures were approved by the Ethics committee of the School of Medicine, of the National Autonomous University of Mexico, license number CIEFM-079-2020.

Mice -Adult (>postnatal day 60) male and female C57/Bl6J WT, PKC-delta (Protein Kinase C delta) - Ai9 (PKCδ-Ai9), were used. Mice were housed in humidity and temperature-controlled vivariums using a normal light cycle with lights on at 7:00 hours and lights off at 19:00 hours. Animals had *ad-libitum* access to standard laboratory chow and water. All procedures were approved by the National Institute of Mental Health Animal Care and Use Committee, NIMH/ACUC approval LCMR-08.

Generation of PKCδ-Ai9-TdTomato mice: To enable the specific visualization of PKCδ-expressing neurons, we generated PKCδ-Ai9-TdTomato reporter mice by crossing heterozygous Prkcd-Cre knock-in mice (B6;129P2-Prkcdtm1.1(cre)Hze/J; Jackson Laboratory, stock #027857) with the Ai9 Cre-dependent reporter line (B6.Cg-Gt(ROSA)26Sortm9(CAG-tdTomato)Hze/J; Jackson Laboratory, stock #007909). In the resulting offspring, Cre recombinase driven by the endogenous Prkcd promoter excises the loxP-flanked STOP cassette at the Rosa26 locus, enabling robust expression of tdTomato fluorescent protein in PKCδ-expressing cells. Double-positive animals were identified by PCR genotyping and used for anatomical and functional analysis.

Immunohistochemistry for light microscopy: Rodents were perfused via the ascending aorta with 0.9% NaCl at room temperature, followed by 4% paraformaldehyde. Brain slices (70 µm) were obtained using a vibratome (Leica VT1200). Slices were washed 3 times in PB, blocked in TBST (Trisma Buffer 0.05M, NaCl 0.9%, 0.3% Triton-X) plus 10% Normal Donkey serum for 2 hrs. Slices were then incubated overnight at 4°C with the following primary antibodies: rabbit anti PACAP (1:2000, BMA, T-4473), guinea pig anti VGLUT1 (1:5000, Chemicon, AB-5905), mouse anti VGLUT2 (1:1000, Chemicon, MAB-5504), guinea pig anti VGLUT2 (1:2000, SySy, 135 404), rabbit anti VAChT (produced and provided by Dr. Lee E Eiden, NIMH, NIH [51]), rabbit anti CGRP (1:1000, Phoenix, H-015-09), mouse anti neurotensin (1:1000, Sigma, SAB-4200703), goat anti calretinin (1:2000, Swant, CG1), diluted in TBST plus 1% NDS. The next day slices were thoroughly washed 3 times in TBST and incubated during two hours in the appropriate secondary biotinylated or fluorescent antibodies from Vector Labs at a concentration of 1:500. The processed sections were examined under bright field using a Nikon Eclipse E600 microscope along with its digital camera for photographic documentation and immunofluorescent reactions were observed using a Stellaris Confocal Microscope from Leica Microsystems.

RNAscope Brains were rapidly dissected, flash-frozen on dry ice, and stored at −80 °C until sectioning for in situ hybridization (ISH). Coronal brain sections (16 µm thick) were obtained

using a cryostat set to −20 °C and mounted directly onto microscope slides. Slides were stored at −80 °C until further processing. RNAscope ISH was performed according to the manufacturer's instructions (Advanced Cell Diagnostics, ACD) and previously published protocols.

Briefly, slides were fixed in 10% neutral-buffered formalin for 20 min at 4 °C, washed twice with PBS (1 min each), and dehydrated through graded ethanol (50%, 70%, and 100%; 5 min each). Slides were stored in 100% ethanol at −20 °C overnight, then air-dried at room temperature (RT) for 10 min. A hydrophobic barrier was drawn around the tissue sections with a PAP pen and allowed to dry for 10–15 min at RT. Sections were incubated with Protease IV for 20 min at RT, rinsed twice in distilled water (ddH_2O), and hybridized with the appropriate probes for 2 h at 40 °C in a HybEZ™ oven (ACD).

For multiplex experiments, the following probes were used (all from ACD): Mm-Grid1-C1 (Cat. No. 552311; target region 396–1301 bp; Accession No. NM_008166.2), Mm-Adcyap1r1-C2 (Cat. No. 409561-C2; target region 4108–5038 bp; Accession No. NM_001025372.1), Mm-Chrna7-C3 (Cat. No. 465161-C3; target region 175–1122 bp; Accession No. NM_007390.3), Mm-Sst-C3 (Cat. No. 404631-C3; target region 18–407 bp; Accession No. NM_009215.1). Following hybridization, slides were washed twice (2 min each) in wash buffer, then sequentially incubated with the amplification reagents in the HybEZ™ oven at 40 °C. Nuclei were counterstained with DAPI (20 s at RT), and slides were coverslipped and stored at 4 °C until imaging. Confocal images were acquired using a Leica Stellaris confocal microscope with a 20× objective and four channels (DAPI, Alexa Fluor 488, 550, and 647).

For duplex experiments, the following probes were used: Mm-Adcyap1 (Cat. No. 405911-C1 and 405911-C2; target region 676–1859 bp; Accession No. NM_009625.2), Mm-Slc17a7-C2 (Cat. No. 416631-C2; target region 464–1415 bp; Accession No. NM_182993.2), Mm-Slc17a6 (Cat. No. 319171-C1 and 319171-C2; target region 1986–2998 bp; Accession No. NM_080853.3), Mm-Calca-C2 (Cat. No. 578771-C2; target region 2–772 bp; Accession No. NM_007587.2), Mm-Chat (Cat. No. 408731-C1; target region 1090–1952 bp; Accession No. NM_009891.2). Following hybridization, slides were washed twice (2 min each) in wash buffer and sequentially incubated with amplification reagents. Cells were counterstained with hematoxylin, coverslipped, and examined under a bright-field microscope.

Ex vivo whole-cell electrophysiology: Ai9-TdTomato-PKCδ mice were used for this study. Anesthesia was induced with pentobarbital, and mice were subsequently decapitated. Brains were rapidly removed and immersed in an ice-cold cutting solution containing (in mM): 92 NMDG, 20 HEPES, 25 glucose, 30 $NaHCO_3$, 2.5 KCl, 1.2 NaH_2PO_4, 10 $MgSO_4$, and 0.5 $CaCl_2$, saturated with 95% O_2/5% CO_2, with an osmolarity of 303–306 mOsm. Following extraction, brains were blocked and mounted in the specimen chamber of a Leica VT1200 vibratome filled with ice-cold cutting solution. Horizontal slices (300 μm thick) containing the central amygdala were sectioned. Slices were then incubated in the same cutting solution at 34°C for 5 minutes. Subsequently, slices were transferred to a chamber containing a holding aCSF solution composed of (in mM): 92 NaCl, 20 HEPES, 25 glucose, 30 $NaHCO_3$, 2.5 KCl, 1.2 NaH_2PO_4, 1

$MgSO_4$, and 2 $CaCl_2$ (303–306 mOsm), saturated with 95% O_2/5% CO_2, and maintained at room temperature for at least 1 hour. Slices remained in this solution until transferred to the recording chamber.

For whole-cell recordings of intrinsic excitability, glass microelectrodes (3–5 MΩ) were filled with an internal solution containing (in mM): 135 K-gluconate, 10 HEPES, 4 KCl, 4 Mg-ATP, 0.3 Na-GTP, and 0.2% biocytin. The capsular region of the central amygdala was identified under low magnification using brightfield and fluorescence illumination. Neurons for recording were selected at high magnification using differential interference contrast (DIC) optics. After achieving whole-cell access and stabilization under voltage clamp, the configuration was switched to current clamp. Series resistance (<20 MΩ) was continuously monitored by measuring the response to a -40 pA current injection. Cells exhibiting a >20% change in series resistance during the recording were excluded from further analysis. Recordings were obtained using a Multiclamp 700B amplifier (Molecular Devices), filtered at 2 kHz, and digitized at 20 kHz with a Digidata 1440A Digitizer (Molecular Devices).

PACAP Application to Brain Slices: to assess the intrinsic excitability of Ai9-PKCδ neurons under current clamp, a current injection protocol was applied, consisting of 1-second steps from -40 pA to 240 pA in 20 pA increments, with 7-second intervals between steps. This protocol was continuously repeated throughout the recording session. Three experimental conditions were evaluated: (1) baseline perfusion with aCSF for 15 minutes, (2) application of aCSF containing 100 nM PACAP for 15 minutes, and (3) a washout period of 15 min with standard aCSF. For each cell, five runs of the protocol in each condition were averaged. For each cell a two-way ANOVA was used to determine whether PACAP application significantly altered the current-induced firing rate. A total of 30 neurons from the capsular region of the central amygdala (CeA) were recorded. After recording, the sections were drop-fixed in 4% PFA in PB for subsequent developing with streptavidin-488 and immunocharacterization.

Transmission Electron Microscopy: Brains from C57BL wild-type mice were sectioned at 40 μm using a Leica VT1000 vibratome. The slices were rinsed in phosphate buffer (PB), incubated in 1% sodium borohydride in PB for 30 minutes to inactivate free aldehyde groups, rinsed again in PB, and then incubated in blocking solution [1% normal goat serum (NGS), 4% bovine serum albumin (BSA) in PB supplemented with 0.02% saponin] for 30 minutes. Sections were then incubated with the following primary antibodies: mouse anti-PKCδ (1:1000, BD Transduction, Cat# 610397); rabbit anti-PACAP (1:50, BMA, Cat# T4473); guinea pig anti-VAChT (1:500, Nittobo Medical, Cat# VAChT-Gp-Af1120); guinea pig anti-VGluT1 (1:500, Nittobo Medical, Cat# VGluT1-GP-Af570); rabbit anti-Dsred (1:1000, Clontech, Cat# 632496); guinea pig anti-VGluT2 (1:500, Nittobo Medical, Cat# VGluT2-GP-Af810); rabbit anti-GluD1C (1:500, Nittobo Medical, Cat# GluD1C-Rb-Af1390); rabbit anti-VGluT2 (1:500, Nittobo Medical, Cat# VGluT2-Rb-Af720-1); and rabbit anti-VAChT (1:500, Nittobo Medical, Cat# VAChT-Rb-Af670). All primary antibodies were diluted in 1% NGS and 4% BSA in PB supplemented with 0.02% saponin, and sections were incubated for 24 hours at 4°C. After rinsing in PB, sections were incubated overnight at 4°C with the corresponding secondary antibodies: Nanogold-Fab' anti-mouse

(1:100, Nanoprobes, Cat# 2002-1ML); Nanogold-Fab' anti-rabbit (1:100, Nanoprobes, Cat# 2004-1ML); Nanogold-Fab' anti-guinea pig (1:100, Nanoprobes, Cat# 2055-ML); and the Vectastain ABC-HRP kits for mouse, rabbit, and guinea pig IgGs (Vector Laboratories, Cat# PK-4002, PK-4001, PK-4007, respectively). Sections were rinsed in PB, then incubated in avidin-biotinylated horseradish peroxidase (HRP) complex in PB for 2 hours at room temperature. After another rinse in PB, sections were post-fixed with 1.5% glutaraldehyde for 10 minutes at room temperature, rinsed in PB, and rinsed in distilled water (to avoid introducing metals to the subsequent steps). Silver enhancement of the gold particles was performed using the HQ Silver Enhancement Kit (Nanoprobes, Cat# 2012) for 7 minutes at room temperature, followed by a PB rinse. Peroxidase activity was then visualized using 0.025% 3,3'-diaminobenzidine (DAB) and 0.003% H_2O_2 in PB for 5–10 minutes. Sections were rinsed with PB, post-fixed in 0.5% osmium tetroxide in PB for 25 minutes, washed in PB and double-distilled water, then stained with 1% uranyl acetate (freshly prepared) for 35 minutes. Dehydration was performed through a graded ethanol series and propylene oxide, followed by flat embedding in Durcupan ACM epoxy resin (Electron Microscopy Sciences, Cat# 14040,Hatfield, PA). Resin blocks were polymerized at 60°C for 2 days. Ultrathin sections (60 nm) were cut from the tissue surface using an Ultramicrotome UC7 (Leica Biosystems, Deerfield, IL) with a DiATOME® diamond knife (Diatome, Hatfield, PA). Sections were collected on formvar-coated single-slot grids and counterstained with Reynolds lead citrate. Imaging was conducted on a Tecnai G2 12 transmission electron microscope**.** (FEI Company, Hillsboro, OR) equipped with a OneView digital camera (Gatan, Pleasanton, CA).

Ultrastructural analysis: Serial ultrathin sections of the capsular region of the central amygdala (CeC) were analyzed. Synaptic contacts were classified according to their morphology and immunolabel and photographed at a magnification of 6,800- 13,000x. In the serial sections, a terminal containing more than 5 immunogold particles was considered as immunopositive. Pictures were adjusted to match contrast and brightness by using Adobe Photoshop (Adobe Systems).

FIB-SEM Methodology: To assess the three-dimensional anatomical characteristics of the Calyx-like contacts, some slices processed immunohistochemistry against PACAP for Electron microscopy, were embedded in Durcupan resin, platinum-covered and positioned in a microscope sample holder. The electron image stack was collected using a ZEISS Crossbeam 550 FIB-SEM (Zeiss Group, Oberkochen, Germany), equipped with a high-performance field emission electron column and a gallium-ion beam column. The ion beam was accelerated at 30 kV for both rough and fine milling. A coarse trench was milled around the protective platinum (Pt) layer using a 15 nA ion current. To prevent curtain artifacts, a thin (~1 μm thick, covering an area of 10 × 10 μm) platinum protective layer was deposited on top of the catalytic layer by injecting a platinum precursor via the gas injection system, using the ion beam at 30 kV and 3 nA.

A chevron-patterned FIB milling registration mark was milled into the protective platinum pad, and an additional FIB-mediated carbon pad was deposited to create a fiducial mark. This allowed for precise control of the slice thickness and ensured accurate 3D alignment of the

image stack, resulting in distortion-free reconstruction. These processes were controlled using ZEISS ATLAS 3D Nanotomography software.

The images were acquired using an Energy-selective Backscattered (EsB) detector with the EsB grid set to 1.5 kV. The SEM beam operated at an accelerating voltage of 3 kV and a current of 1.5 nA, which was optimized for sequential removal of thin slices during the nanotomography process. The total depth of the trench created by this procedure was 20 μm. Backscattered electron images were captured in the X-Y plane, while the sequential removal of slices occurred along the Z-axis. For tomography, a pixel size of 20 nm × 10 nm was used, corresponding to a slice thickness of 20 nm.

The raw FIB-SEM dataset comprised 1568 images, which were cropped and processed into a single volume image. The final volume image was reconstructed and analyzed and segmented using ORS Dragonfly software.

SI Table 1.Antibodies used in this study

Primary antibodies

Target	Host Species	Dilution	Source	Catalog Number
For electron microscopy				
DsRed	Rabbit	1:1000	Clontech	632496
GluD1C	Rabbit	1:500	Nittobo Medical	GluD1C-Rb-Af1390
PKCδ	Mouse	1:1000	BD Transduction	610397
PACAP	Rabbit	1:50	BMA	T4473
VAChT	Guinea pig	1:500	Nittobo Medical	VAChT-Gp-Af1120
VAChT	Rabbit	1:500	Nittobo Medical	VAChT-Rb-Af670
VAChT	Rabbit	n/a	Provided by Dr. Lee Eiden (NIMH, NIH)	n/a
VGluT1	Guinea pig	1:500	Nittobo Medical	VGluT1-GP-Af570
VGluT2	Guinea pig	1:500	Nittobo Medical	VGluT2-GP-Af810
VGluT2	Rabbit	1:500	Nittobo Medical	VGluT2-Rb-Af720-1
For light microscopy				
PACAP	Rabbit	1:2000	BMA	T-4473
VGluT1	Guinea pig	1:5000	Chemicon	AB-5905
VGluT2	Mouse	1:1000	Chemicon	MAB-5504
VGluT2	Guinea pig	1:2000	Synaptic Systems	135 404
CGRP	Rabbit	1:1000	Phoenix Pharmaceuticals	H-015-09
Neurotensin	Mouse	1:1000	Sigma	SAB-4200703
Calretinin	Goat	1:2000	Swant	CG1

Secondary antibodies

Reagent	Target	Dilution	Source	Catalog Number
Nanogold-Fab' anti-mouse	Mouse	1:100	Nanoprobes	2002-1ML
Nanogold-Fab' anti-rabbit	Rabbit	1:100	Nanoprobes	2004-1ML
Nanogold-Fab' anti-guinea pig	Guinea pig	1:100	Nanoprobes	2055-ML
Biotinylated Goat anti-rabbit	Rabbit	1:500	Vector Laboratories	BA-1000
DyLight 405 Goat anti-rabbit	Rabbit	1:500	Jackson ImmunoResearch	111-475-003
Alexa Fluor 488 Donkey anti-goat	Goat	1:500	ThermoFisher	A-11055
Alexa Fluor 594 goat anti mouse	mouse	1:500	Jackson ImmunoResearch	115-585-003